A Unified Nonlinear Multiscale Interaction Model of Pacific–North American Teleconnection Patterns

DEHAI LUO, YAO GE, AND WENQI ZHANG

Key Laboratory of Regional Climate-Environment for Temperate East Asia, Institute of Atmospheric Physics, Chinese Academy of Sciences, and University of Chinese Academy of Sciences, Beijing, China

AIGUO DAI

Department of Atmospheric and Environmental Sciences, University at Albany, State University of New York, Albany, New York

(Manuscript received 6 November 2019, in final form 9 January 2020)

ABSTRACT

In this paper, reanalysis data are first analyzed to reveal that the individual negative (positive)-phase Pacific–North American pattern (PNA) or PNA$^-$ (PNA$^+$) has a lifetime of 10–20 days, is characterized by strong (weak) westerly jet stream meanders, and exhibits clear wave train structures, whereas the PNA$^-$ with rapid retrogression tends to have longer lifetime and larger amplitude than the PNA$^+$ with slow retrogression. In contrast, the wave train structure of the North Atlantic Oscillation (NAO) is less distinct, and the positive (negative)-phase NAO shows eastward (westward) movement around a higher latitude than the PNA. Moreover, it is found that the PNA wave train occurs under a larger background meridional potential vorticity gradient (PV_y) over the North Pacific than that over the North Atlantic for the NAO. A unified nonlinear multiscale interaction (UNMI) model is then developed to explain why the PNA as a nonlinear wave packet has such characteristics and its large difference from the NAO. The model results reveal that the larger background PV_y for the PNA (due to its location at lower latitudes) leads to its larger energy dispersion and weaker nonlinearity than the NAO, thus explaining why the PNA (NAO) is largely a linear (nonlinear) process with a strong (weak) wave train structure, though it is regarded as a nonlinear initial-value problem. The smaller PV_y for the PNA$^-$ than for the PNA$^+$ leads to lower energy dispersion and stronger nonlinearity for PNA$^-$, which allows it to maintain larger amplitude and have a longer lifetime than the PNA$^+$. Thus, the difference in the background PV_y is responsible for the asymmetry between the two phases of PNA and the difference between the PNA and NAO.

1. Introduction

The Pacific–North American teleconnection pattern (PNA) is one of the most important atmospheric low-frequency modes in the Northern Hemisphere midlatitudes (Dickson and Namias 1976; Wallace and Gutzler 1981; Feldstein 2002; Franzke and Feldstein 2005; Franzke et al. 2011). While the PNA shows a wave train with four centers that propagates from the subtropical North Pacific to the southeastern United States (Barnston and Livezey 1987; Feldstein 2002), it exhibits a tilted dipole meridional structure with a very weak southern node over the North Pacific. Because the PNA and its change can significantly influence North American weather and climate (Harnik et al. 2016; Singh et al. 2016; H. Wang et al. 2017; S.-Y. Wang et al. 2017; Schulte and Lee 2017; Swain et al. 2018; Yu and Lin 2019), the triggering mechanism of the PNA events with a subseasonal time scale of 10–20 days (Feldstein 2002) has been an important research topic (Hoskins and Karoly 1981; Cash and Lee 2001; Franzke and Feldstein 2005; Franzke et al. 2011; Baxter and Nigam 2013; Song 2018).

Many studies have revealed that while the PNA is associated with the thermal forcing in the tropics (Hoskins and Karoly 1981) and El Niño–Southern Oscillation (ENSO) (Horel and Wallace 1981), it arises mainly from the forcing of successive traveling

Supplemental information related to this paper is available at the Journals Online website: https://doi.org/10.1175/JAS-D-19-0312.s1.

Corresponding author: Dr. Dehai Luo, ldh@mail.iap.ac.cn

DOI: 10.1175/JAS-D-19-0312.1

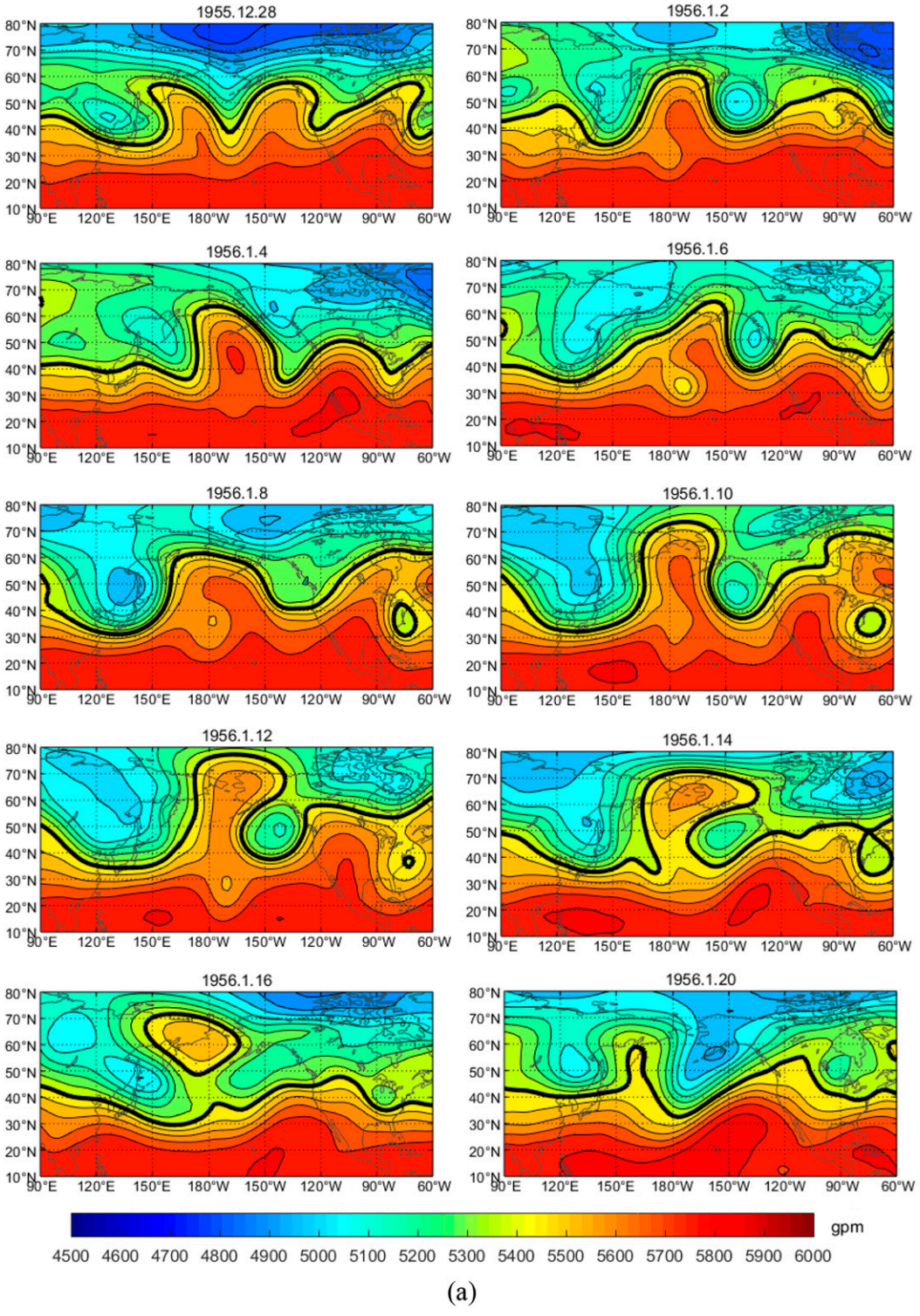

FIG. 1. Instantaneous daily Z500 [contour interval (CI) = 80 gpm] fields of (a) PNA^- events during the periods from 28 Dec 1955 to 20 Jan 1956 and (b) PNA^+ events occurring over North Pacific during 8–22 Dec 2002. The thick black line denotes the 5440-gpm contour line.

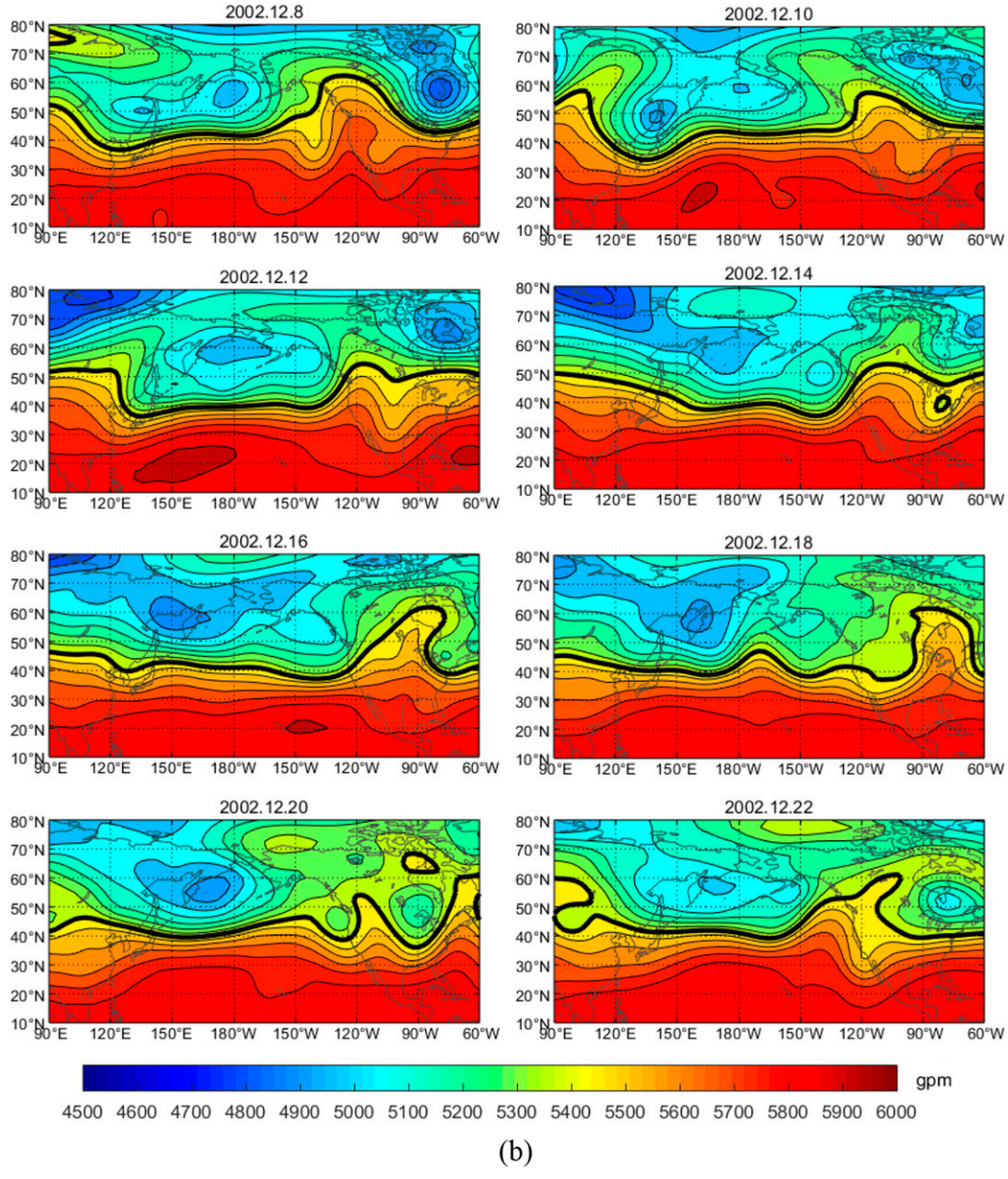

FIG. 1. (*Continued*)

synoptic-scale eddies through eddy momentum fluxes (Lau 1988; Lau and Nath 1991; Feldstein 2002; Franzke et al. 2011; Song 2018). In a diagnostic study, Feldstein (2002) found that the PNA is dominated by a linear process. Song (2018) used a simplified model to examine the role of synoptic-scale eddies in the PNA onset by separating synoptic-scale eddies into preexisting and deformed eddies following Luo (2000) and Luo et al. (2007). While the vorticity budget diagnostic studies by Feldstein (2002) and Mori and Watanabe (2008) can reveal that the PNA life cycle is a weakly nonlinear or a strongly linear process, they cannot tell us what factor leads to such a strongly linear process or why the nonlinear interaction between the low-frequency components of the PNA is so weak that the linear process is dominant. Moreover, why individual PNA events last for about 2 weeks but not shorter or longer, and why the PNA shows a strong asymmetry between its two phases have not been answered so far, because no analytical or theoretical models have been developed to describe the life cycle of individual PNA events. Because the background wind, PNA and synoptic-scale eddies are often coupled together, this makes it difficult to use numerical models and the vorticity

budget or streamfunction tendency equation to identify their causal linkage. The unified nonlinear multiscale interaction (UNMI) model developed by Luo et al. (2007, 2015, 2018) provides a possible tool for examining this issue. Thus, this UNMI model has the potential to address this question because it considers low-frequency modes such as atmospheric blocking or NAO events as a nonlinear initial-value problem (Luo 2000, 2005; Luo et al. 2007).

The UNMI model used here is an extension of the nonlinear multiscale interaction (NMI) model of atmospheric blocking proposed by Luo (2000, 2005). In this NMI model, the blocking is generated from the interactions among the basic flow, planetary-scale waves, and synoptic-scale eddies that are separated into preexisting and deformed synoptic-scale eddies, and the planetary and synoptic-scale zonal waves are separated in deriving the analytic solutions under a zonal-scale separation assumption (Luo 2000, 2005; Luo and Li 2000; Luo et al. 2001, 2014, 2019). The UNMI model can describe the life cycle of not only atmospheric blocking, but also individual NAO events, with the negative-phase NAO (NAO^-) being considered to resemble a blocking flow (Luo et al. 2007, 2015, 2018). Thus, the UNMI model unifies atmospheric blocking and NAO events into one model. In the UNMI model, the deformed eddies play only a secondary role in the generation and maintenance of blocking and NAO patterns, suggesting that the eddy straining (i.e., synoptic-scale wave breaking) is not a key process for the establishment of atmospheric blocking or NAO.

Because the unfiltered daily geopotential height field of the PNA^- (PNA^+) event (Fig. 1) bears a striking resemblance to that of the NAO^- (NAO^+) event (Luo et al. 2007) and the PNA can also be similarly considered as an initial-value problem, it is feasible to use the UNMI model to examine the basic physics of the PNA life cycle by extending the UNMI model to include the effect of background wind fields over the North Pacific. In this extended UNMI model, we can establish the linkage between the background wind field and PNA by considering the variation of the background meridional potential vorticity (PV) gradient induced by the background wind change, while the PNA is driven by preexisting synoptic-scale eddies and the PNA induces a zonal-mean wind change. The most important advantage of this UNMI model is that it provides an inverse ratio rule of the energy dispersion–nonlinearity relation for describing the linear and nonlinear behaviors of atmospheric low-frequency (10–20 day) dipole modes, such as atmospheric blocking (Luo et al. 2019). This inverse ratio rule says that the energy dispersion is proportional to the background meridional PV gradient (PV_y), whereas the nonlinearity is proportional to the inverse of PV_y. When the North Pacific background wind condition is considered in this model, the energy dispersion–nonlinearity inverse ratio rule obtained from the UNMI model should apply to the case of the PNA event. This motivated us to apply the extended UNMI model to explain the basic characteristics (including the life cycle) of the PNA events and to reveal the physical cause of the asymmetry of the PNA between its two phases. To our knowledge, the modified UNMI model presented in this study represents the first theoretical or analytical model of the PNA.

We first describe the data and method in section 2. The description of the extended UNMI model is given in section 3. Composite results of the PNA events are presented in section 4 based on reanalysis data. The model results about the impact of the background zonal wind or meridional PV gradient on the PNA are further presented in section 5. A comparison between the PNA and NAO is made in section 6. Conclusions and discussion are given in the final section.

2. Data and method

Here, we used daily data for 500-hPa geopotential height (Z500) and zonal wind (U500), and surface air temperature (SAT) from the National Centers for Environmental Prediction–National Center for Atmospheric Research (NCEP–NCAR) reanalysis (Kalnay et al. 1996) on a 2.5° × 2.5° latitude–longitude grid for boreal winter [from December to February (DJF)] from December 1950–February 1951 to December 2017–February 2018 (1950–2017). The anomaly for each variable at each grid point is derived by subtracting its local mean seasonal cycle and linear trend. The daily PNA index is constructed by projecting the daily (0000 UTC) 500-hPa height anomalies over the Northern Hemisphere onto the loading pattern of the PNA that is defined as the second leading mode of rotated empirical orthogonal function (REOF) analysis of monthly mean Z500 during the 1950–2000 period. The daily NAO index has a similar definition, but the loading pattern of the NAO is defined as the first leading REOF mode of monthly mean Z500 during the 1950–2000 period. The daily PNA and NAO indices were obtained from the NOAA Climate Prediction Center (https://www.cpc.ncep.noaa.gov/). A PNA^+ (PNA^-) event is defined to have taken place if the daily PNA index exceeds 1.25 (−1.25) standard deviations above (below) its mean value for at least 3 consecutive days. For NAO events, we use the same definition with the PNA index. We also excluded the

PNA (~21.6%) and NAO (~14.6%) events if their indices are nonmonotonic during their growth and decay phases. Here, a nonmonotonic event is defined if there are two peaks and their time interval is less than 10 days. To quantify the life cycle of a PNA or an NAO event, we define the day when the daily PNA or NAO index reaches its maximum as the lag 0 day, and then average the life cycle over all the selected events to derive a composite life cycle for PNA or NAO events.

3. Description of the UNMI model

While the excitation of the PNA is related to large-scale forcing (Hoskins and Karoly 1981; Horel and Wallace 1981; Mori and Watanabe 2008) and zonally asymmetric climatological flow (Branstator 1992), it seems that the vorticity flux from the synoptic-scale eddies plays a major role in the generation and maintenance of the PNA (Lau 1988; Branstator 1992; Feldstein 2002; Franzke and Feldstein 2005; Franzke et al. 2011). In fact, the zonally asymmetric climatological flow can influence the PNA mainly via the generation of synoptic-scale eddies due to barotropic–baroclinic instability (Frederiksen 1983). To some extent, it is thought that the PNA can indirectly gain its kinetic energy from the background flow via synoptic-scale eddy feedback (Branstator 1992). In this paper, to isolate the effect of zonally symmetric or asymmetric background flow over the North Pacific on the PNA life cycle and to emphasize the key role of PV_y related to the meridional distribution and strength of background zonal winds in the linear and nonlinear evolution of the PNA, we assume that synoptic-scale eddies have existed before the PNA onset and the background flow prior to the PNA onset is prespecified and does not produce additional synoptic-scale eddies to directly influence the PNA. Because the preexisting background flow is changed as a response to the PNA life cycle once the PNA occurs, as mentioned below, it is difficult to infer if the changing background flow leads to the PNA life cycle or vice versa in model and reanalysis data diagnostic studies. But our model here seems to be able to avoid this difficulty.

Here, we use the UNMI model for NAO or blocking events of Luo et al. (2018, 2019), but extend it to include a nonuniform background zonal wind over the North Pacific. To help understand the model, below we present a complete description of the model with much of the text and most of the equations taken from Luo et al. (2018, 2019) and other earlier papers by Luo et al. with some modifications to adapt the model to the PNA case.

As revealed below, the preexisting background zonal wind over the North Pacific prior to PNA onset shows a zonally asymmetric zonal flow distribution and then is referred to as a zonally asymmetric background flow, hereafter. Considering a zonally asymmetric background flow $\overline{\psi}(x, y)$, we decompose the nondimensional total streamfunction field ψ_T, scaled by characteristic length $\tilde{L}$ ($\approx$1000 km) and velocity $\tilde{U}$ ($\approx 10\,\mathrm{m\,s^{-1}}$), of the PNA event into three parts: $\psi_T = \overline{\psi}(x, y) + \psi + \psi'$, where $\overline{\psi}(x, y)$ is the background flow streamfunction normalized by $\tilde{L}\tilde{U}$ that is maintained by stationary external forcing, ψ is the planetary-scale PNA anomaly with zonal wavenumber k, and ψ' is the synoptic-scale eddies with zonal wavenumbers $\tilde{k}_j$ (j = 1, 2, 3, ...). Under the zonal-scale separation assumption $k \ll \tilde{k}_j$ (Luo 2000, 2005; Luo et al. 2014, 2018), the nondimensional planetary- and synoptic-scale PV equations of the UNMI model in a nonuniform zonally varying background flow $\overline{\psi}(x, y)$ ($U = -\partial\overline{\psi}/\partial y$ and $V = \partial\overline{\psi}/\partial x$) in a β-channel plane with a width of L_y are obtained as

$$\left(\frac{\partial}{\partial t} + U\frac{\partial}{\partial x}\right)(\nabla^2\psi - F\psi) + J(\psi, \nabla^2\psi) + \mathrm{PV}_y\frac{\partial\psi}{\partial x} = -\nabla\cdot(\mathbf{v}'q')_P - V\frac{\partial\nabla^2\psi}{\partial y} - \frac{\partial\psi}{\partial y}\left(\frac{\partial^2 U}{\partial x\partial y} - \frac{\partial^2 V}{\partial x^2}\right), \quad (1a)$$

$$\left(\frac{\partial}{\partial t} + U\frac{\partial}{\partial x}\right)(\nabla^2\psi' - F\psi') + \mathrm{PV}_y\frac{\partial\psi'}{\partial x} = -J(\psi', \nabla^2\psi) - J(\psi, \nabla^2\psi') - V\frac{\partial\nabla^2\psi'}{\partial y} - \frac{\partial\psi'}{\partial y}\left(\frac{\partial^2 U}{\partial x\partial y} - \frac{\partial^2 V}{\partial x^2}\right) + \nabla^2\psi_S^*, \quad (1b)$$

where $\mathrm{PV}_y = \beta + V_{xy} - U_{yy} + FU$ is the meridional gradient of the background PV in a nonuniform zonally varying basic flow with $(U, V) = (-\partial\overline{\psi}/\partial y, \partial\overline{\psi}/\partial x)$, $U_y = \partial U/\partial y$, $U_{yy} = \partial^2 U/\partial y^2$, $V_{xy} = \partial^2 V/\partial x\partial y$, $F = (\tilde{L}/R_d)^2$, R_d is the radius of Rossby deformation, $-J(\overline{\psi}, \nabla^2\overline{\psi})_P$ is a stationary term that has a very weak projection into the PNA anomaly and is balanced by the stationary external forcing, $\nabla\cdot(\mathbf{v}'q')_P = J(\psi', \nabla^2\psi')_P$ and $\mathbf{v}' = (u', v') = (-\partial\psi'/\partial y, \partial\psi'/\partial x)$, $\nabla\cdot(\mathbf{v}'q')_P$ represents the planetary-scale component of the eddy vorticity flux divergence $\nabla\cdot(\mathbf{v}'q')$ induced by synoptic-scale eddies ψ' with its relative vorticity $q' = \nabla^2\psi'$. Here, $\nabla\cdot(\mathbf{v}'q')_P$ is assumed to have the same spatial scale as that of the PNA anomaly ψ. Note that $\beta = \beta_0\tilde{L}^2/\tilde{U}$ is the nondimensional meridional gradient of the Coriolis parameter at a reference latitude φ_0, $\nabla^2\psi_S^*$ is the synoptic-scale vorticity source that maintains preexisting synoptic-scale

eddies prior to the PNA onset (Luo 2005; Luo et al. 2018, 2019).

When a slowly varying background zonal flow exists and it is zonally uniform or $\overline{\psi} = \overline{\psi}(y)$, one can have $\mathrm{PV}_y = \beta - U_{yy} + FU$, $U = U(y)$, and $V = 0$. Thus, Eq. (1) in a zonally asymmetric background flow is an extension of the UNMI model obtained by Luo et al. (2019) for a blocking system. The analytical solution to Eq. (1) can be derived using the Wentzel–Kramers–Brillouin (WKB) method when the assumption $\psi' \approx \psi_1' + \psi_2'$ is used (where ψ_1' denotes the preexisting synoptic-scale eddies with two wavenumbers $\tilde{k}_1$ and $\tilde{k}_2$ prior to the PNA onset and ψ_2' represents the deformed eddies due to the feedback of the intensified PNA on preexisting synoptic eddies). One can obtain $\partial q/\partial t \approx -\nabla \cdot (\mathbf{v}_1' q_1')_P$ because of $\psi_2' \approx 0$, $\mathbf{v}' \approx \mathbf{v}_1' = (-\partial\psi_1'/\partial y, \partial\psi_1'/\partial x)$, and $q' \approx q_1' = \nabla^2\psi_1'$ during the initial stage ($t \sim 0$) of the PNA development, where $-\nabla \cdot (\mathbf{v}_1' q_1')_P$ is the preexisting eddy forcing induced by the preexisting eddies. It is noted that the PNA event with zonal and meridional wavenumbers k and m, respectively, can be driven by $-\nabla \cdot (\mathbf{v}_1' q_1')_P$, if q represents the PV anomaly of the PNA and $-\nabla \cdot (\mathbf{v}_1' q_1')_P$ has the same spatial structure as that of q. This process may be referred to as the eddy-PNA matching mechanism, which is also held for the formation of blocking and NAO events (Luo 2000, 2005; Luo et al. 2014, 2015, 2018, 2019).

Assuming that $\overline{\psi}(x, y)$ has slower variations in the zonal and meridional directions than the carrier wave of the PNA. Using the WKB method, the total atmospheric streamfunction field of an eddy-driven PNA event derived from Eq. (1) in a nonuniform slowly varying background flow in a first variable form can be expressed as

$$\psi_T = \overline{\psi}(x,y) + \psi + \psi' = \psi_P + \psi', \tag{2a}$$

$$\psi_P = \overline{\psi}(x,y) + \psi \approx \overline{\psi}(x,y) + \psi_{\mathrm{PNA}} + \psi_m, \tag{2b}$$

$$\psi_{\mathrm{PNA}} = B\sqrt{\frac{2}{L_y}}\exp[i(kx - \omega t)]\sin(my) + \mathrm{cc}, \tag{2c}$$

$$\psi_m = -|B|^2 \sum_{n=1}^{\infty} q_n g_n \cos(n + 1/2)my, \tag{2d}$$

$$\psi' \approx \psi_1' + \psi_2', \tag{2e}$$

$$\psi_1' = f_0(x)\{\alpha_1 \exp[i(\tilde{k}_1 x - \tilde{\omega}_1 t)] + \alpha_2 \exp[i(\tilde{k}_2 x - \tilde{\omega}_2 t)]\}\sin\left(\frac{m}{2}y\right) + \mathrm{cc}, \tag{2f}$$

$$\begin{aligned}\psi_2' = &-\frac{m}{4}\sqrt{\frac{2}{L_y}}Bf_0(x)\sum_{j=1}^{2} Q_j\alpha_j \exp\{i[(\tilde{k}_j + k)x - (\tilde{\omega}_j + \omega)t]\}\left[p_j \sin\left(\frac{3m}{2}y\right) + r_j \sin\left(\frac{m}{2}y\right)\right] \\ &+\frac{m}{4}\sqrt{\frac{2}{L_y}}B^* f_0(x)\sum_{j=1}^{2} Q_j\alpha_j \exp\{i[(\tilde{k}_j - k)x - (\tilde{\omega}_j - \omega)t]\}\left[s_j \sin\left(\frac{3m}{2}y\right) + h_j \sin\left(\frac{m}{2}y\right)\right] + \mathrm{cc},\end{aligned} \tag{2g}$$

$$i\left(\frac{\partial B}{\partial t} + C_g\frac{\partial B}{\partial x}\right) + \lambda\frac{\partial^2 B}{\partial x^2} + \delta|B|^2 B + Gf_0(x)^2 \exp[-i(\Delta kx + \Delta\omega t)] = 0, \tag{2h}$$

where ψ_T is the total streamfunction field of the PNA life cycle, ψ_P denotes the streamfunction field of the planetary-scale component of the PNA with its planetary-scale anomaly ψ_{PNA} (i.e., the removal of ψ_m and $\overline{\psi}(x, y)$ from ψ_P), ψ_m is the PNA-induced zonal-mean zonal wind change during the PNA life cycle, which reflects the variation of the background flow [$\overline{\psi}(x, y)$ plus ψ_m], and B in Eq. (2h) denotes the complex amplitude of the PNA wave packet. In Eq. (2e), ψ' is the synoptic-scale eddy streamfunction composed of two parts: ψ_1' and ψ_2', where ψ_1' denotes the streamfunction anomaly of the preexisting synoptic-scale eddies and ψ_2' represents the streamfunction anomaly of deformed eddies.

In Eq. (2h), we note that $\Delta k = k - (\tilde{k}_2 - \tilde{k}_1)$ or $\Delta\omega = \tilde{\omega}_2 - \tilde{\omega}_1 - \omega$ denotes the difference of the zonal wavenumber or frequency between the PNA anomaly ψ_{PNA} and preexisting eddy forcing $-\nabla \cdot (\mathbf{v}_1' q_1')_P$, $\omega = Uk - [\mathrm{PV}_y k/(k^2 + m^2 + F)]$, $C_g = \partial\omega/\partial k = U - \mathrm{PV}_y(m^2 + F - k^2)/(k^2 + m^2 + F)^2$ is the group velocity, $\tilde{\omega}_j = U\tilde{k}_j - \mathrm{PV}_y\tilde{k}_j/(\tilde{k}_j^2 + m^2/4 + F)$ ($j = 1, 2$) is the frequency of preexisting synoptic-scale eddies ψ_1', $|B|^2 = B^*B$, B^* is the complex conjugate of B, $q_n = q_{Nn}/\mathrm{PV}_y$ is the coefficient of the mean zonal wind change ψ_m and cc denotes the complex conjugate of its preceding term. Note that $\lambda = \lambda_0\mathrm{PV}_y$ with $\lambda_0 = [3(m^2 + F) - k^2]k/(k^2 + m^2 + F)^3$ ($\lambda_0 > 0$) is the linear dispersion term, $\delta = \delta_N/\mathrm{PV}_y$ ($\delta_N > 0$) is the nonlinearity strength, $k = 2k_0$,

TABLE 1. Values of given parameters used to calculate the extended UNMI model solution.

Parameters	Value
Nondimensional zonal wavenumber k of the PNA anomaly	$k = 2/(6.371\cos\varphi_0)$
Nondimensional zonal wavenumber $\tilde{k}_1$ of preexisting synoptic-scale eddies	$\tilde{k}_1 = 8/(6.371\cos\varphi_0)$
Nondimensional zonal wavenumber $\tilde{k}_2$ of preexisting synoptic-scale eddies	$\tilde{k}_2 = 10/(6.371\cos\varphi_0)$
Reference latitude φ_0	35°N
Nondimensional width L_y of the β channel	4.5
Characteristic horizontal length $\tilde{L}$	10^6 m
Characteristic horizontal wind speed $\tilde{U}$	10 m s^{-1}
μ	0 to 1.5
ε	0.24
Zonal location x_T of preexisting synoptic-scale eddies	−2.87/4 to 2.87/2
Amplitude a_0 of preexisting synoptic-scale eddies	0.25

$k_0 = 1/(6.371\cos\varphi_0)$, $m = \pm 2\pi/L_y$, $\alpha_1 = 1$, $\alpha_2 = \alpha$, $\tilde{k}_j = nk_0 + (-1)^j\Delta n k_0$ ($j = 1, 2$), n is the positive integer (e.g., $n = 9$), and Δn is chosen to be 1 and represents the difference between $\tilde{k}_1$ and $\tilde{k}_2$. In Eqs. (2f)–(2h), $f_0(x) = a_0\exp[-\mu\varepsilon^2(x + x_T)^2]$ represents the spatial distribution of the slowly varying eddy amplitude, $\mu > 0$, $\varepsilon \ll 1.0$ is a small parameter and x_T is the zonal location of the maximum eddy amplitude. In Eqs. (2d)–(2h), δ_N, q_{Nn}, g_n, Q_j p_j, r_j, s_j, h_j, and G can be found in the appendix.

As in Luo et al. (2019), a high-order split-step Fourier scheme (Muslu and Erbay 2005) is also used to solve Eq. (2h) to obtain the spatiotemporal solution of the PNA amplitude B for given parameters in Table 1 and initial conditions as a nonlinear initial-value problem. In the extended UNMI model, the PNA anomaly may be regarded as a nonlinear wave packet that is described by a forced nonlinear Schrödinger (NLS) equation [Eq. (2h)]. The solution (2c) represents the negative (positive) phase of PNA or PNA$^-$ (PNA$^+$) when $\alpha = -1$ and $m = -2\pi/L_y$ ($\alpha = 1$ and $m = 2\pi/L_y$) are chosen. We also find $-\Delta\omega = \mathrm{PV}_y[\tilde{k}_2/(\tilde{k}_2^2 + m^2/4 + F) - \tilde{k}_1/(\tilde{k}_1^2 + m^2/4 + F) - k/(k^2 + m^2 + F)]$ for $k = \tilde{k}_2 - \tilde{k}_1$. It is inferred from our analytical solution that the larger-PV$_y$ region corresponds to an area of stronger energy dispersion, weaker nonlinearity and short-lived eddy forcing because there are $\lambda \propto \mathrm{PV}_y$, $\delta \propto 1/\mathrm{PV}_y$, and $\Delta\omega \propto \mathrm{PV}_y$ as found in Luo et al. (2019) for a blocking system. Clearly, $\lambda = \lambda_0\mathrm{PV}_y$ and $\delta = \delta_N/\mathrm{PV}_y$ or $\lambda \propto 1/\delta$ always hold even for a zonally asymmetric background flow and the PNA system, which is also appropriate for the NAO. Thus, the energy dispersion of the PNA system is proportional to the inverse of the nonlinearity. This is the so-called inverse ratio rule of the energy dispersion–nonlinearity relation first derived by Luo et al. (2019) for the blocking system. These relations imply that the PNA$^+$ tends to be more strongly dispersive and have a shorter lifetime (larger $\Delta\omega$) than the PNA$^-$ because the PNA$^+$ corresponds to a larger PV$_y$ over the North Pacific midlatitudes. Moreover, because $U(x, y)$ and PV$_y$ are the function of x and y, B in Eq. (2h) should be the function of x, y, and t, though the variations in the x and y directions have been assumed to be slowly varying.

The nonlinear phase speed C_{NP} of the PNA can be obtained as (Luo et al. 2019)

$$C_{\mathrm{NP}} = U - \frac{\mathrm{PV}_y}{k^2 + m^2 + F} - \frac{\delta_N M_0^2}{2k\mathrm{PV}_y}, \tag{3}$$

where $M_0 = |B|_{\max}$ represents the maximum amplitude of the daily PNA anomaly. One can see how the PNA anomaly moves during the life cycle of the PNA event from Eq. (3) if U, PV$_y$, and the amplitude M_0 of the northern pole of PNA are known. This formula can also be applied to the cases of blocking and NAO. Thus, calculating the nonlinear phase speed C_{NP} of the PNA wave packet from Eq. (3) can allow us to infer how the movement or propagation of the PNA wave train depends on its phase and associated environment conditions over the North Pacific.

4. Characteristics of the PNA

a. *Individual PNA events and their connection to jet stream*

To shed an insight into the dynamics of individual PNA events, it is useful to examine the unfiltered daily fields from selected PNA$^-$ and PNA$^+$ events. Figure 1a shows a PNA$^-$ event during the period from 28 December 1955 to 20 January 1956, while Fig. 1b shows a PNA$^+$ event during 8–22 December 2002. It is seen that the PNA$^-$ event shows a life cycle from the growth and maintenance to the decay with a lifetime of about 20 days. The evolution of this PNA$^-$ looks like the formation process of a North Pacific blocking, which is characterized by the presence of a meandering westerly jet stream consisting of isolated small-scale cyclonic and anticyclonic vortices within the blocking region (Fig. 1a) (Berggren et al. 1949). We also note that the growth and westward movement of the PNA$^-$ (28 December

1955 to 10 January 1956) is linked to the northward (southward) displacement of intensified ridges mainly over the North Pacific (deepened troughs mainly to the west and east of the Pacific ridge) or associated warm (cold) air mass that resembles a cyclonic wave breaking (CWB). Thus, the generation and maintenance of the PNA^- is associated with the presence of CWB.

Moreover, intense small-scale troughs and ridges are seen during the initiation stage of the PNA^+ event (8 and 10 December in Fig. 1b). But along with the intensification of the PNA^+, these small-scale troughs and ridges are absorbed by the mean zonal flow to strengthen the zonal flow due to the presence of an intensified large-scale cyclonic-over-anticyclonic dipole over the North Pacific midlatitudes (12, 14, and 16 December), which resembles the behavior of weakened small-scale ridges and troughs during the NAO^+ episode. This PNA^+ event also shows a westward movement and has a time scale of about 14 days, consistent with previous findings (e.g., Feldstein 2002). Overall, the individual PNA^- (PNA^+) event corresponds to the presence (absence) of CWB or blocking flow over the North Pacific. Thus, the generation of the PNA is linked to synoptic-scale wave breaking (Franzke et al. 2011). However, why the PNA life cycle has the above behavior and a lifetime of about two weeks (10–20 days) are not be explained in previous studies. Our extended UNMI model can be used to investigate these issues.

b. *Composite results of PNA events*

During the 68 winters from December 1950 to February 2017, there were 77 PNA^+ and 68 PNA^- events according to the above PNA definition. Figure 2a shows their composite evolution (i.e., average over all the events for each lag time) of the daily PNA index for the two phases. It is seen that the *e*-folding time scale of the PNA^+ and PNA^- is around 10 and 12 days, respectively, with the difference being statistically significant at the 95% confidence level. The PNA^- also has larger amplitude than the PNA^+. Thus, on average the PNA^- events tend to have larger amplitude and longer lifetime than the PNA^+ events. Figures 2b and 2c show time-mean composite Z500 anomalies averaged from lag −5 to 5 days (with lag 0 corresponding to the peak of the PNA index) for the two phases. Clearly, over the North Pacific the positive Z500 anomaly of the PNA^- (Fig. 2c) is stronger than the negative Z500 anomaly of the PNA^+ (Fig. 2b). Also, the northern pole of the PNA over the central North Pacific is much stronger than the southern pole centered on about 20°N for both phases. We further show the time–longitude evolution of composite daily Z500 anomalies averaged over 35°–55°N in Figs. 2d and 2e for the two phases. It is interesting to find that both the PNA^- and PNA^+ anomalies show retrogression (i.e., westward movements), with the PNA^- (Fig. 2e) having a faster mean westward movement speed of about $-2.9\,m\,s^{-1}$ than the PNA^+ with a mean westward speed of $-1.5\,m\,s^{-1}$ (Fig. 2d). We also see that the Z500 anomaly peaks on lag −1 day for the PNA^- and PNA^+ (Figs. 2d,e); thus, it leads the peak of the daily PNA index by about 1 day.

Figures 3a and 3b show the temporal evolution of composite daily Z500 anomaly fields for the two phases of the PNA. The PNA Z500 anomaly field exhibits a quadrupole structure from the subtropical North Pacific to North America during its evolution. The positive Z500 anomaly over the west coast of North America is weak from lag −8 to −4 days (Fig. 3a) when the North Pacific center is still developing but becomes strong from lag −2 to +2 days when the North Pacific center is very strong. This reflects a strong energy dispersion of the PNA^+ leading to an intensification of downstream positive height anomaly over the west coast of North America. The similar features are found for the PNA^- (Fig. 3b). Thus, the growth and maintenance of the PNA^+ or PNA^- can be accompanied by a strong downstream energy dispersion, even though the energy dispersion of the PNA^+ is stronger, as noted below. A significant difference between the PNA^+ and PNA^- is that a positive (negative) Z500 anomaly appears over the west coast of North America for the PNA^+ (PNA^-), which leads to a warm west–cold east dipole of SAT anomalies over North America during the decaying phase (from lag 0 to 4 days) for the PNA^+ (Fig. 3a) but a cold west–warm east dipole SAT anomaly over North America during the mature and decay phases (from lag −2 to 4 days) for the PNA^- (Fig. 3b). The PNA^+ can partly help explain the 2013/14 drought in California (S.-Y. Wang et al. 2017). We also note that the northern pole of the PNA^- shifts northward with its intensification (Fig. 3b), but the meridional movement of the PNA^+ is hardly seen (Fig. 3a). In addition, it is found that during the beginning stage the PNA^- is zonally more isolated than the PNA^+ (Fig. 3 for day −8). It implies that the initial PNA^- also has weaker energy dispersion than the initial PNA^+. This result is not noted in previous studies.

Here, we define $D_I = (H_P - H_A)/H_P$ as a daily index to quantify whether the PNA wave packet exhibits a strong energy dispersion as in Luo et al. (2018), where H_P is the absolute value of the domain-averaged daily Z500 anomaly over an area of 5° latitude × 5° longitude around the anticyclonic (cyclonic) center of the PNA^- (PNA^+) over the North Pacific, and H_A is the absolute value of the domain-averaged daily Z500 anomaly over

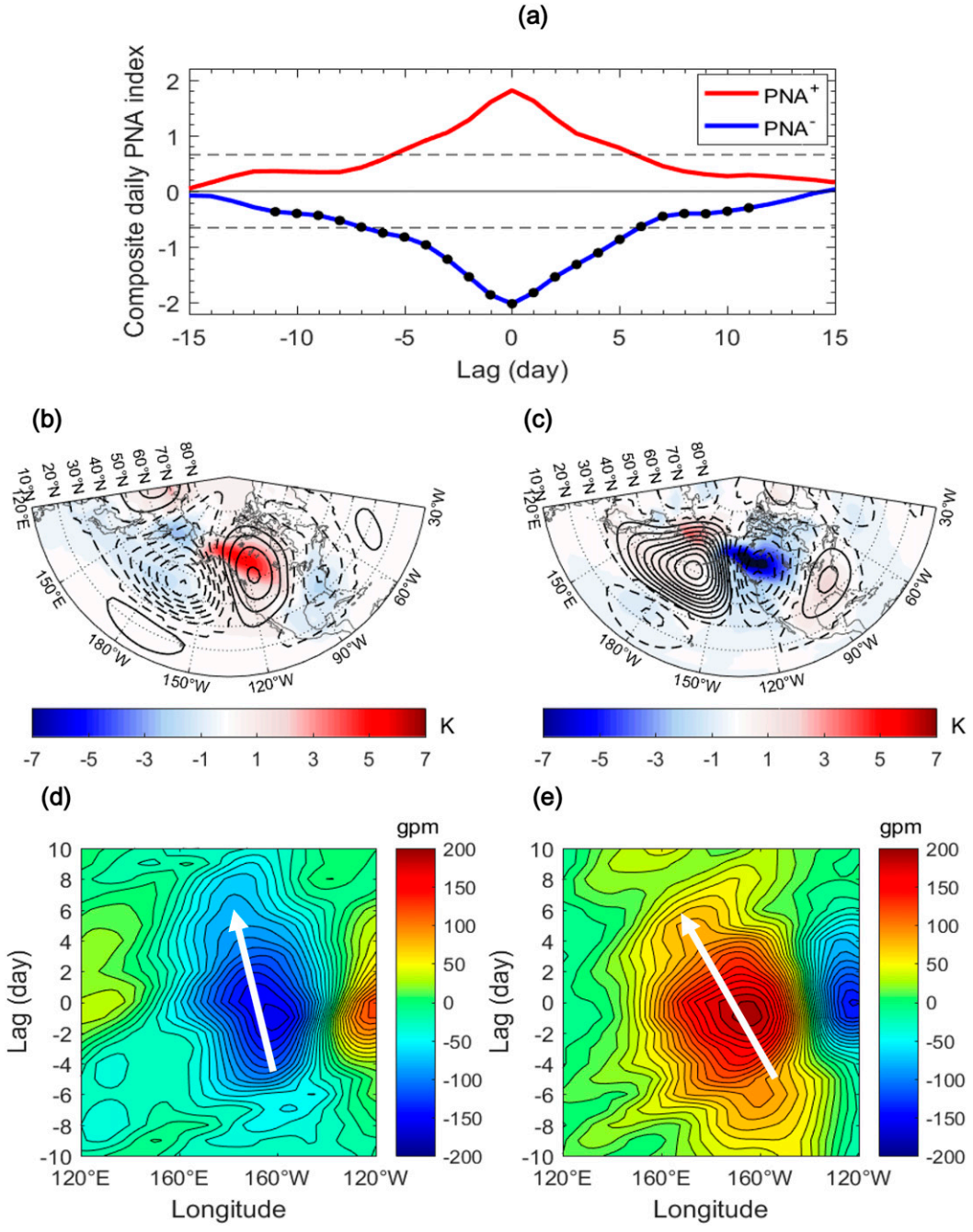

FIG. 2. (a) Composite daily PNA indices for the PNA^+ (red line) and PNA^- (blue line) events in winter during 1950–2017, with the dashed line representing the *e*-folding line of the index and the black dots denoting that the amplitude difference between the two phases is statistically significant at the 95% confidence level based on 5000 Monte Carlo simulations. (b) The time-mean composite daily Z500 (contours; CI = 20 gpm) and SAT (color shading; K) anomalies averaged from lag −5 to 5 days of the PNA index shown in (a) for PNA^+ cases. (c) As in (b), but for PNA^- events. In (b) and (c), only statistically significant anomalies (at the 5% level based on the two-sided Student's *t* test) are shown by the contours or color shading. (d) Time–longitude evolution of latitude-averaged composite daily Z500 anomalies (gpm) over 35°–55°N during the PNA life cycle for PNA^+ events. (e) As in (d), but for PNA^- events. In (d) and (e), the arrow denotes the movement direction.

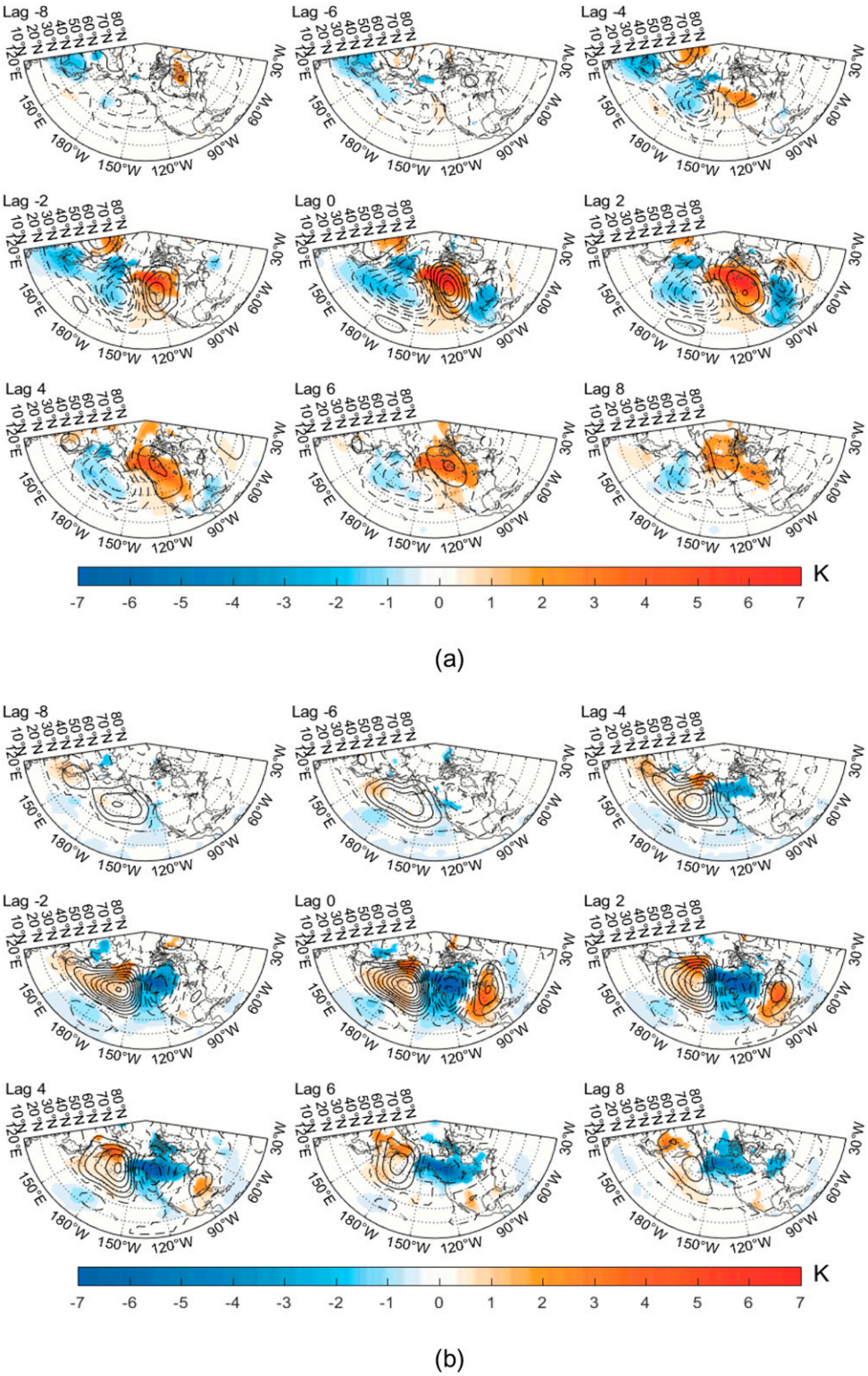

FIG. 3. Temporal evolution of the composite daily Z500 (contours; CI = 30 gpm) and SAT (color shading; K) anomalies for (a) PNA^+ and (b) PNA^- events from lag −8 to +8 days during 1950–2017. Only statistically significant anomalies (at the 5% level) are shown by the contours or color shading.

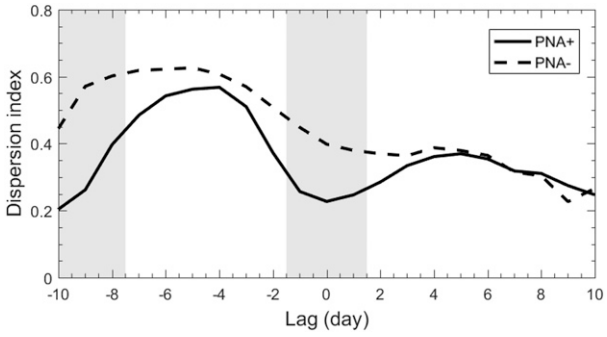

FIG. 4. Temporal evolution of the daily dispersion index D_I during the PNA life cycle for PNA$^+$ (solid line) and PNA$^-$ (dashed line) events during 1950–2017. The gray shading denotes the difference between the two lines being significant at the 5% level based on 5000 Monte Carlo simulations.

an area of 5° latitude × 5° longitude around the cyclonic (anticyclonic) center over North America. This index describes the difference of the Z500 anomaly amplitude between upstream and downstream, thus reflecting the energy dispersion strength of the PNA. When $H_A = 0$, the PNA cannot disperse its energy toward downstream because the Z500 anomaly vanishes over the North America. In this case, one can have $D_I = 1$. However, when H_A is nonzero or when there is a Z500 anomaly over the North America, $D_I < 1.0$ exists. This case represents that the PNA can disperse its energy toward the North America. Thus, when D_I is large (small), the PNA has a weak (strong) energy dispersion.

Figure 4 shows the temporal variation of the composite daily dispersion index D_I of the PNA events. It is seen that during the early stage (from lag −10 to −8 days) of the PNA, D_I is smaller for the PNA$^+$ than for the PNA$^-$. This suggests that the PNA$^+$ has a stronger energy dispersion than the PNA$^-$ even during the initiation phase of the PNA. We further see that for the PNA$^+$ D_I increases sharply from lag −10 to −6, but decreases rapidly from lag −4 to −1, and then increases again from lag 0 to +4; while the change for the PNA$^-$ is more muted (Fig. 4). Nevertheless, D_I is lower for PNA$^+$ than for PNA$^-$ prior to lag +5. Thus, the PNA$^+$ has a stronger energy dispersion than PNA$^-$ during most of their life cycle, although they can have reduced energy dispersion when the PNA amplitude is intensified. It is noted that while the PNA has its peak amplitude at lag −1 (Figs. 2d,e), strong energy dispersion occurs mainly during the growing (before lag −7 days) and decaying (from lag −1 to 2 days) phases of the PNA. As noted below, such an energy dispersion is probably related to the differences in the background PV$_y$ and initial PNA conditions between the two phases of the PNA.

We also see that the time evolution of the PNA energy dispersion is different from that of the NAO energy dispersion (Fig. 4e of Luo et al. 2018), where the strong energy dispersion of the NAO occurs mainly during the decaying stage. Since D_I is lower after lag −1 than earlier stages, the energy dispersion of the PNA also shows a distinct asymmetry between its growing and decaying phases. Thus, the above results suggest that the PNA$^+$ has stronger energy dispersion than the PNA$^-$ during its growing, mature and decaying phases. Such an asymmetry of the PNA energy dispersion was not investigated in previous studies, but it can be further examined here based on the UNMI model as described above.

c. *Linkage of the PNA energy dispersion to zonal winds and PV$_y$*

To reveal the physical cause of the PNA asymmetry, here we will examine whether the differences in the PNA's duration, energy dispersion and movement are related to the differences in the background conditions between its two phases. Figure 5 shows that the U500 and PV$_y$ (i.e., PV$_y = \beta - U_{yy} + FU$) anomalies during the mature phase (lag −5 to +5) of the PNA mainly occur in the latitude band of 25°–45°N, and they are intensified (weakened) over the North Pacific within this latitude band during the PNA$^+$ (PNA$^-$) events. Here, we calculated the time-mean U500 and PV$_y$ averaged from lag −20 to −10 days prior to the PNA onset as the background condition of the PNA and show the results in Fig. 6. It is found that the composite background U500 and PV$_y$ over the North Pacific (mainly within 25°–45°N, 180°–130°W) are stronger for the PNA$^+$ (Figs. 6a,d) than for the PNA$^-$ (Figs. 6b,e). This point can be clearly seen from the PNA$^+$ minus PNA$^-$ difference as shown in Figs. 6c and 6f, which also show significant positive differences over the latitudes 25°–45°N and significant negative differences over the latitudes 45°–60°N of Eurasia and Pacific. Thus, it is possible that the short duration and strong energy dispersion of the PNA$^+$ may be related to the strong (weak) U500 and PV$_y$ over the North Pacific lower latitudes 25°–45°N (mid–high latitudes 45°–60°N) prior to its onset.

We also see from Fig. 6 that the background U500 and PV$_y$ over the North Pacific have a strong zonal asymmetry. The background flow over the North Atlantic also shows a strong zonal asymmetry (see Fig. S1 in the online supplemental material). But such a background flow asymmetry does not allow the NAO to have a strong energy dispersion because PV$_y$ is small over the North Atlantic. As noted below, it is the magnitude of the background PV$_y$, rather than the zonal asymmetry of the background flow, that determines the energy dispersion change of the PNA life cycle.

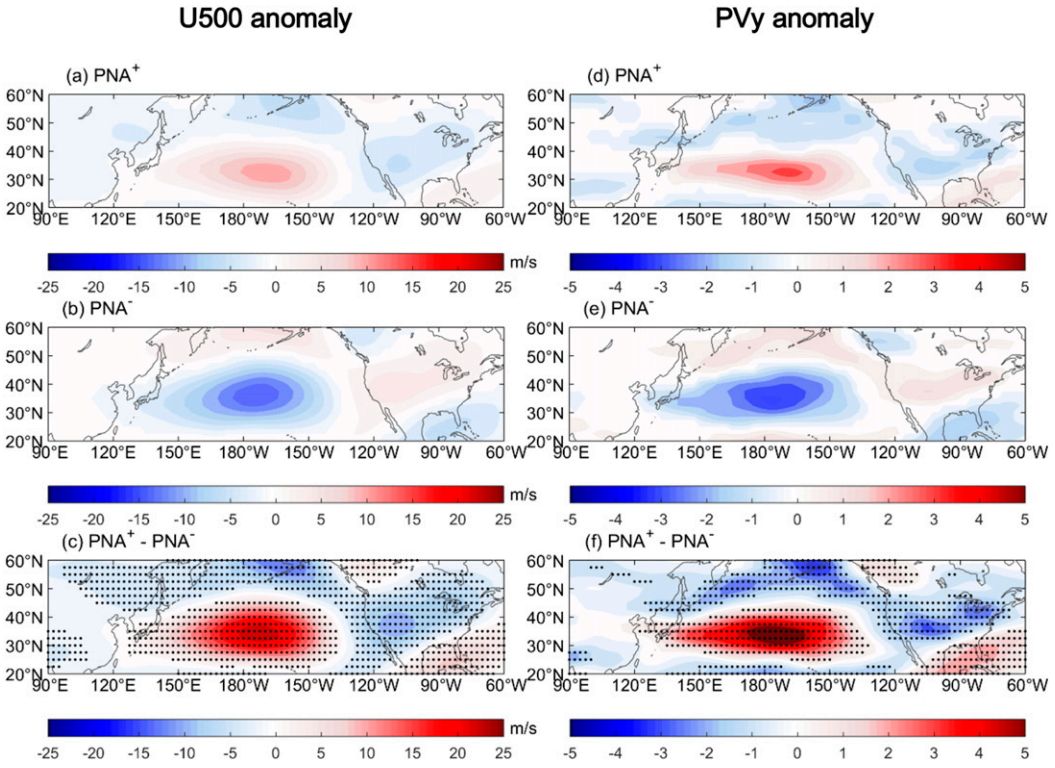

FIG. 5. Time-mean composite daily (left) 500-hPa zonal wind ($m\,s^{-1}$) and (right) PV_y anomalies averaged from lag −5 to 5 days for (a),(d) PNA^+, (b),(e) PNA^-, and (c),(f) PNA^+ minus PNA^-. The dots denote that the difference is statistically significant at the 95% confidence level based on the two-sided Student's *t* test.

d. Composite results of NAO events and their difference with the PNA

Similar to Fig. 2, we show the temporal evolution of the composite daily NAO indices for 78 NAO^+ and 80 NAO^- events and the corresponding time-mean composite daily Z500 and SAT anomalies from lag −5 to 5 days during 1950–2017 in Fig. 7 based on the definition of individual NAO event in section 2. It is found that the *e*-folding time scale of the NAO^+ and NAO^- events is around 9 and 11 days, respectively, with the NAO^- having a larger amplitude than the NAO^+. Their duration difference (based on the *e*-folding time scale) is statistically significant at the 5% level. A comparison with Fig. 2a reveals that the asymmetry between the two phases of the PNA and NAO is similar. However, the time-mean composite daily Z500 anomalies of the NAO events (Figs. 7b,c) show a less distinct wave train structure than that for the PNA (Figs. 2b,c), which is consistent with NAO's weak energy dispersion. For the NAO, there is a weak positive (negative) Z500 anomaly in the downstream side of the high-latitude North Atlantic for NAO^+ (NAO^-), with the positive Z500 anomaly over Eurasia being more intense for the NAO^+ (Fig. 7b) than the Eurasian negative Z500 anomaly for the NAO^- (Fig. 7c). This weak anomaly over Eurasia reflects NAO's weaker energy dispersion than the PNA. Moreover, the NAO's northern pole is centered around 65°N, which is farther north than that of the PNA's northern pole (around 45°N for the PNA^+ and 50°N for the PNA^-, Figs. 2b and 2c). Figures 7d and 7e show that the NAO^+ (NAO^-) exhibits an eastward (westward) movement with a speed of about $3.4\,m\,s^{-1}$ ($-3.8\,m\,s^{-1}$), in contrast to PNA's westward movement for both phases (Figs. 2d,e). Why the PNA has strong asymmetry and why such an asymmetry is different from that of the NAO will be further examined by using the extended UNMI model below.

5. Theoretical model results

a. Background U500 and PV_y

Figure 8 shows the meridional distributions of zonal winds and associated PV_y averaged from lag −20 to −10 days prior to the PNA onset over the North Pacific, which are considered as the background condition of the PNA. It is noted that the background U500 and PV_y are stronger over 25°–45°N in the North Pacific prior to the onset of the PNA^+ and over 45°–60°N in the North

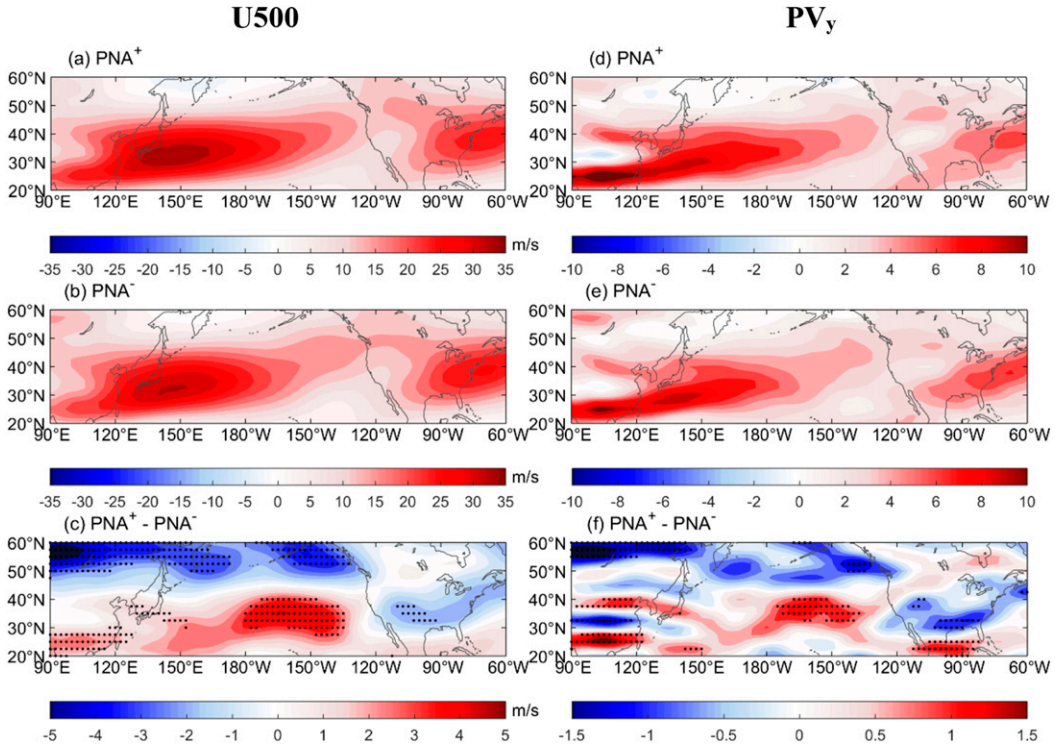

FIG. 6. Time-mean composite daily (left) 500-hPa zonal winds (U500; m s^{-1}) and (right) nondimensional PV$_y$ averaged from lag −20 to −10 days for (a),(d) PNA$^+$, (b),(e) PNA$^-$, and (c),(f) PNA$^+$ minus PNA$^-$. The dots denote that the difference is statistically significant at the 95% confidence level for or the two-sided Student's *t* test.

Atlantic prior to the onset of the NAO$^+$ than for the PNA$^-$ and NAO$^-$. The calculation shows that the vertically (1000–200 hPa) averaged prior zonal wind and PV$_y$ are basically the same as those of 500 hPa in intensity and meridional distribution (not shown). Furthermore, the U500 and PV$_y$ peaks also shift from around 48°N prior to the NAO$^-$ to around 52°N prior to the NAO$^+$, while the peaks are at lower latitudes prior to both the PNA$^-$ and PNA$^+$ and their meridional shift is less distinct (Fig. 8). Consistent with NAO's northern pole being farther north than PNA's, the U500 and PV$_y$ peaks are also located farther north prior to the NAO than prior to the PNA. These results suggest that the differences between the PNA and NAO may be related to their different background conditions in zonal winds and PV$_y$ prior to their onset. Below, we examine the effect of different background zonal winds or PV$_y$ on the PNA evolution using the extended UNMI model described in section 3.

b. Dispersion and nonlinearity of PNA and NAO

While previous diagnostic studies (e.g., Feldstein 2002; Mori and Watanabe 2008) revealed that the PNA life cycle tends to be a linear process, they did not show what factor leads to the linear behavior of the PNA or the nonlinear behavior of the NAO. Here, we show that a large (small) background PV$_y$ over the North Pacific (North Atlantic) is a key factor for determining whether the PNA (NAO) is a linear (nonlinear) process. This finding has not been shown in previous studies. Below, we provide a theoretical explanation on the difference between the linear and nonlinear behaviors of the PNA and NAO.

As mentioned above, because $\lambda = \lambda_0 \mathrm{PV}_y$ and $\delta = \delta_N/\mathrm{PV}_y$ or the inverse ratio rule $\lambda \propto 1/\delta$ hold for the PNA system, we can apply this inverse ratio rule to explain the difference between the PNA and NAO. Because the northern pole of the composite NAO (PNA) Z500 anomaly is centered around 65°N (45°–50°N) (Figs. 2, 7), the NAO (PNA) corresponds to a smaller (larger) PV$_y$ background (Figs. 8b,d). As a result, the energy dispersion parameter $\lambda = \lambda_0 \mathrm{PV}_y$ is larger because of PV$_y$ being larger over the North Pacific while the nonlinearity parameter $\delta = \delta_N/\mathrm{PV}_y$ is smaller for the PNA than for the NAO. Of course, the difference that the climatological mean PV$_y$ is larger in the Pacific than in the Atlantic may be related to the difference of tropical forcing and topography. Clearly, whether the PNA (NAO) shows a strong (weak) energy dispersion crucially depends on the magnitude of PV$_y$ over the North

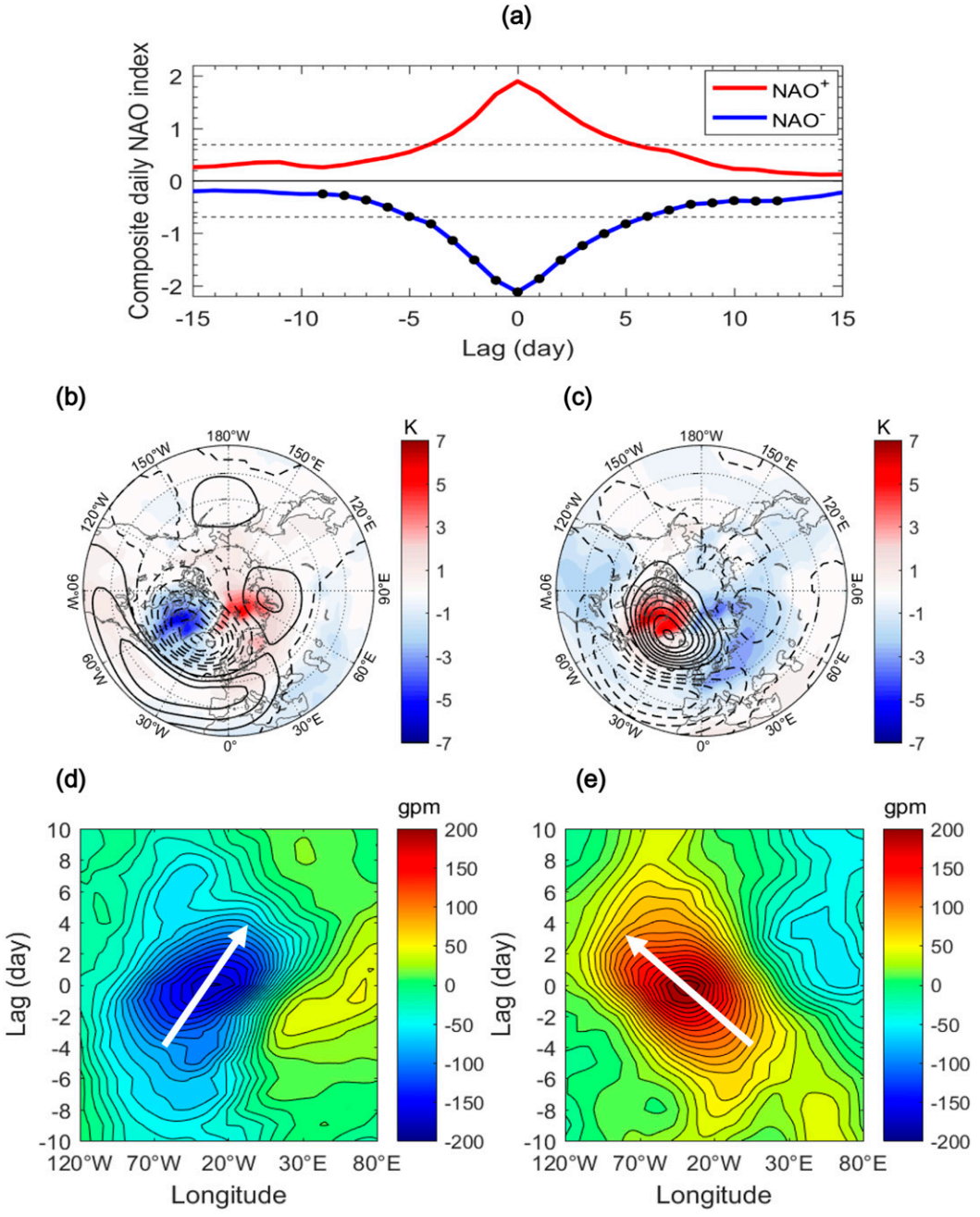

FIG. 7. (a) Composite daily NAO indices for the NAO^+ (red line) and NAO^- (blue line) events in winter during 1950–2017, with the dashed line representing the *e*-folding line of the index and the black dots denoting that the amplitude difference between the two phases is statistically significant at the 95% confidence level based on 5000 Monte Carlo simulations. (b) The time-mean composite daily Z500 (contours; CI = 20 gpm) and SAT (color shading; K) anomalies averaged from lag −5 to 5 days of the NAO index for NAO^+ cases over 30°–90°N (c) As in (b), but for NAO^- events. In (b) and (c), only statistically significant anomalies (at the 5% level based on the two-sided Student's *t* test) are shown by the contours or color shading. (d) Time–longitude evolution of latitude-averaged composite daily Z500 anomalies (gpm) over 55°–75°N during the NAO life cycle for NAO^+ events. (e) As in (d), but for NAO^- events. In (d) and (e), the arrow denotes the movement direction.

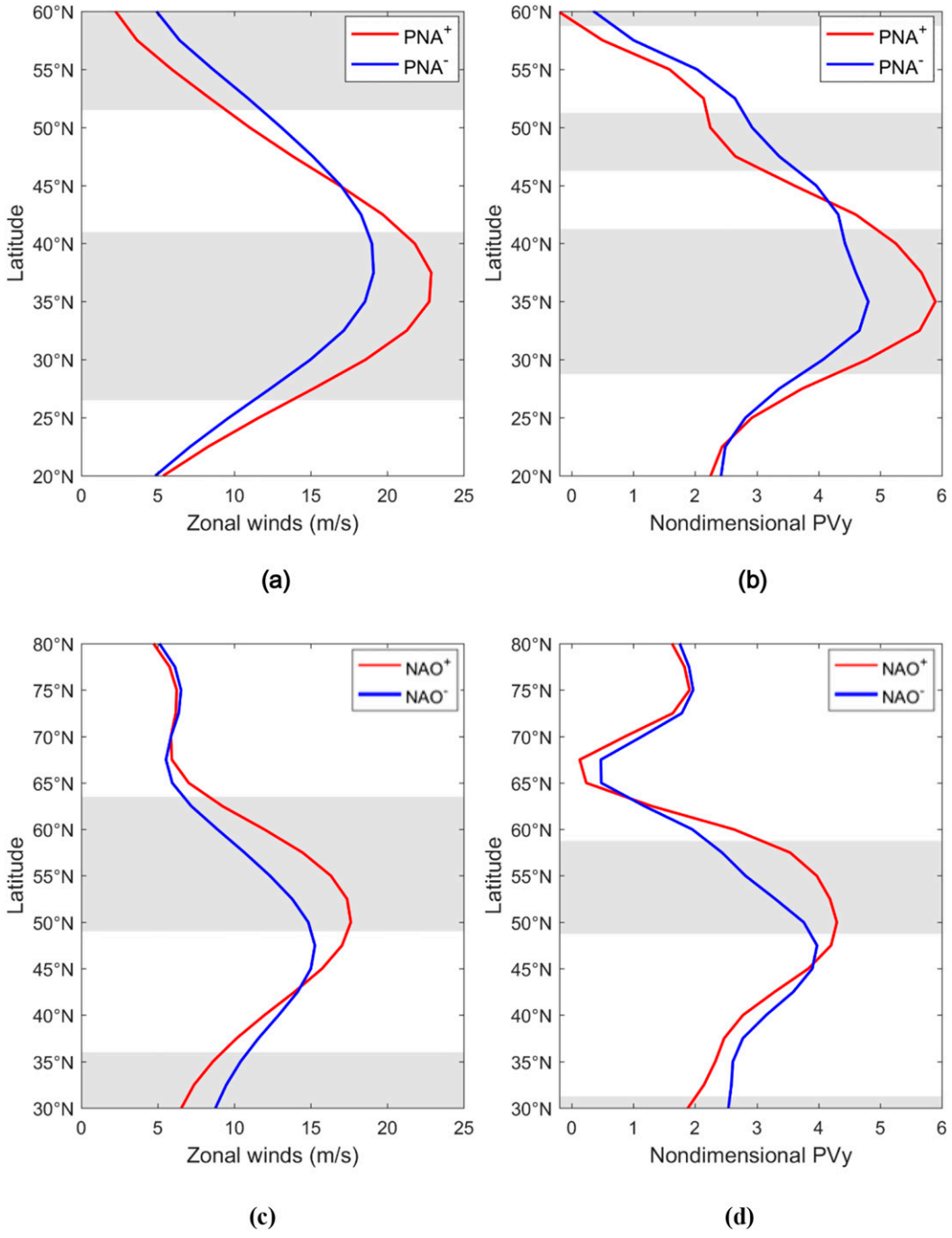

FIG. 8. Variations of time-mean composite daily (a),(c) 500-hPa zonal winds and (b),(d) nondimensional PV_y averaged from lag −20 to −10 days with the latitude for (a),(b) PNA^+ (red line) and PNA^- (blue line) over the region 180°–140°W and (c),(d) NAO^+ (red line) and NAO^- (blue line) over the region 50°W–0°. The gray shading denotes that the difference of the zonal winds or nondimensional PV_y between the PNA^+ and PNA^- is significant at the 95% confidence level based on a Monte Carlo test with 5000 simulations.

Pacific (North Atlantic) rather than on whether the background flow has a strong zonal asymmetry. Equation (2h) is reduced to $i[(\partial B/\partial t) + C_g(\partial B/\partial x)] + \lambda(\partial^2 B/\partial x^2) + Gf_0(x)^2 \exp[-i(\Delta kx + \Delta\omega t)] \approx 0$ if $\delta \approx 0$ is assumed for $PV_y \to \infty$. This extreme case represents a forced linear equation, which reflects a linear process with a very strong dispersion and a very weak nonlinearity and corresponds to a wave train structure. We do not calculate this case

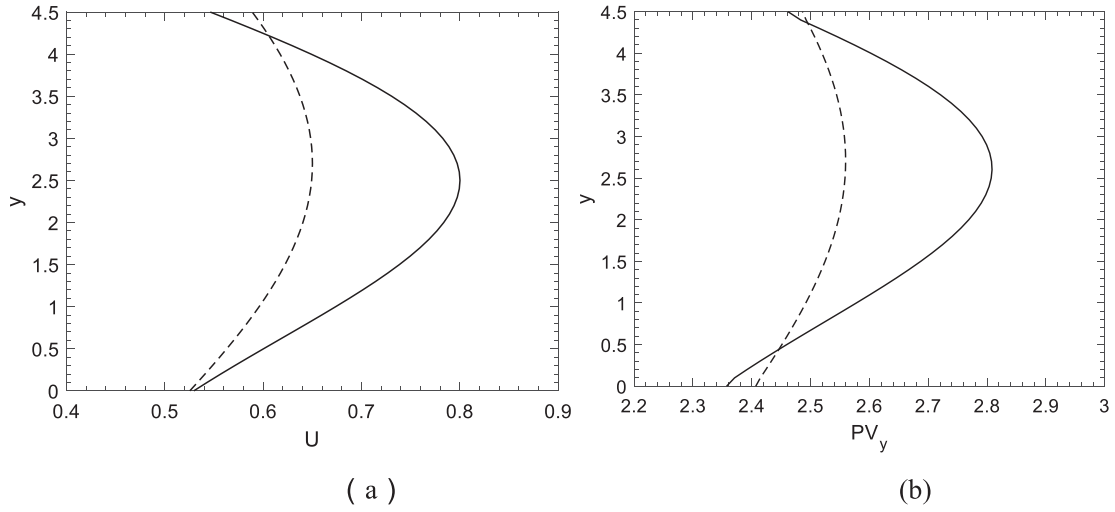

FIG. 9. Meridional profiles of (a) background zonal wind and (b) PV$_y$ of $U = U_0 + \Delta u(y - y_0)^2 e^{-\gamma(y-y_1)^2}$ for PNA$^+$ (solid line; $U_0 = 0.8$, $\Delta u = -0.07$, $\gamma = 0.05$, $y_0 = 2.5$, and $y_1 = 3.1$) and PNA$^-$ (dashed line; $U_0 = 0.65$, $\Delta u = -0.02$, $\gamma = 0.02$, $y_0 = 2.7$, and $y_1 = 2.8$).

here. For the PNA case, because PV$_y$ is relatively large over the North Pacific for the PNA$^+$ and PNA$^-$, the life cycle of the PNA is mainly controlled by a strongly linear (or a strong dispersion) process because of δ being relatively small.

On the other hand, because PV$_y$ is smaller for the PNA$^-$ than for the PNA$^+$, it is inevitable that the PNA$^+$ has stronger energy dispersion than the PNA$^-$, thus explaining the data result in Fig. 4. Compared with the PNA, the NAO has smaller λ (i.e., weaker dispersion) but larger δ (i.e., stronger nonlinearity) because PV$_y$ is smaller over the North Atlantic. Thus, the life cycle of the NAO is dominated by a nonlinear process unlike the PNA. Naturally, the NAO has inevitably a zonally isolated dipole solution in that δ is large (i.e., a nonlinear process) because of PV$_y$ being small over the North Atlantic. However, because δ is small (i.e., a linear process) due to PV$_y$ being large over the North Pacific, ψ_{PNA} has inevitably a wavelike structure solution. Thus, a wave train structure like the PNA is easily seen over the North Pacific. The results of the theoretical analysis provide an explanation about why the PNA anomaly often behaves as a wave train structure, and why the wave train structure is less evident for the NAO anomaly or why the NAO easily shows an isolated dipole structure. Namely, the above theoretical results can clearly explain the NAO with a zonally isolated dipole structure being the dominant mode over the North Atlantic, but the PNA-like wave train being the dominant mode over the North Pacific. Below, we further use the extended UNMI model to examine the temporal evolution of the PNA and its energy dispersion by solving Eq. (2h) for given parameters in Table 1.

c. *Movement, duration, and energy dispersion*

We should first examine whether the extended UNMI model can capture the main features of observed PNA events in movement, duration and energy dispersion before revealing the physical cause of the PNA asymmetry between its two phases and its difference with the NAO. In this paper, we only present the result for a case with an idealized zonally uniform background flow whose meridional distribution resembles that in Fig. 8a. The effect of the zonally asymmetric background flow $U(x, y)$ is also calculated and the results are shown in the supplementary file (Figs. S2–S9). It is found that the results for the case with a zonally asymmetric background flow largely resemble those for a zonally uniform background flow presented here.

We also note that the strength of $U(y)$ in Fig. 9 is lower than that of U500 prior to the PNA onset, because we consider a barotropic case in this paper. Such a choice is qualitatively reasonable in that the vertically averaged prior zonal wind may be crudely considered as a barotropic background wind. In fact, as noted below, while the strength and meridional distribution of $U(y)$ can influence the temporal evolution of the PNA, the basic characteristics of the PNA are not changed with the strength (i.e., meridionally averaged value) of $U(y)$. Here, we assume that $U(y)$ (the normalized zonal wind in units of $\tilde{U} \approx 10\,\mathrm{m\,s^{-1}}$) has a meridional distribution (Fig. 9a) of $U = U_0 + \Delta u(y - y_0)^2 e^{-\gamma(y-y_1)^2}$, which is close to that in Fig. 8a, where U_0 denotes the uniform part of the background westerly wind, and Δu, y_0, γ, and y_1 represent the parameters of the background zonal wind.

In our extended UNMI model, $y = 0$ ($y = L_y$) denotes the southern (northern) boundary of the dipole component of the PNA over the North Pacific. Because the zero line between the anticyclonic and cyclonic anomalies of the PNA dipole is located near 30°N and $U(y)$ peaks at about 35°N, the peak of $U(y)$ should be assumed to be located in the north side of $y = L_y/2 = 2.25$ (2250 km in a dimensional unit) where the center of the PNA dipole exists. By adjusting the values of U_0, Δu, y_0, γ, and y_1, $U(y)$ may be allowed to be close to the basic wind of the PNA$^+$ or PNA$^-$ from the reanalysis data. Considering $U_0 = 0.8$ (corresponding to $\sim 8\,\mathrm{m\,s^{-1}}$) $\Delta u = -0.07$ (corresponding to about $-0.7\,\mathrm{m\,s^{-1}}$), $\gamma = 0.05$, $y_0 = 2.5$ (corresponding to 2500 km), and $y_1 = 3.1$ (corresponding to 3100 km) as the basic westerly wind parameters of the PNA$^+$ and $U_0 = 0.65$, $\Delta u = -0.02$, $\gamma = 0.02$, $y_0 = 2.7$ (corresponding to 2700 km), and $y_1 = 2.8$ (corresponding to 2800 km) for PNA$^-$, we show the variation of the corresponding PV$_y$ with the normalized meridional distance y (in units of 1000 km) in Fig. 9b. It is found that although $U(y)$ in Fig. 9a is highly idealized, its meridional distribution is similar to the observed structure of the basic zonal wind for the PNA$^+$ or PNA$^-$. Also, the meridional distribution of PV$_y$ in Fig. 9b resembles that shown in Fig. 8b. In the following, we will use these specified $U(y)$ and PV$_y$ and the extended UNMI model to examine how the PNA depends on the background conditions.

In Eq. (2), B represents the nondimensional amplitude of the PNA anomaly ψ_{PNA} scaled by $\tilde{U}\tilde{L}$. Because the initial PNA$^-$ (PNA$^+$) anomaly shows a more (less) zonally localized zonal distribution, we choose $B(x, y, 0) = 0.4\exp[-\nu(y - \tilde{y}_0)^2]e^{-\gamma_1 x^2}$ as the initial amplitude of the PNA, where $\tilde{y}_0 > 0$ is the meridional position of the northern pole of the PNA at $x = 0$, $\nu > 0$ represents that the northern pole of the initial PNA dipole is stronger than its southern pole and $\gamma_1 > 0$ denotes the nonuniform zonal distribution of the initial PNA. Since the downstream anomaly of the initial PNA$^-$ (Fig. 3b for lag -8) is weaker than that of the initial PNA$^+$ (Fig. 3a for lag -8), γ_1 in $B(x, y, 0) = 0.4\exp[-\nu(y - \tilde{y}_0)^2]e^{-\gamma_1 x^2}$ must satisfy $\gamma_1 > 0$ so that $B(x, y, 0)$ with $\gamma_1 > 0$ represents a more zonally localized amplitude of the initial PNA$^-$. But $\gamma_1 = 0$ is allowed for the PNA$^+$ because the initial PNA$^+$ has a strong wave train structure and shows a less zonally localized distribution. Based on the above consideration, we may choose $\tilde{y}_0 = 0.75L_y$, $\nu = 0.15$, and $\gamma_1 = 0$ ($\gamma_1 = 0.005$) as the initial value of the PNA$^+$ (PNA$^-$) event. We further take the parameters for the preexisting synoptic-scale eddies same as in Table 1, but allow $\mu = 0.2$ and $x_T = 2.87/4$. For this case, the preexisting eddy forcing is located in the upstream side of the initial PNA. To make a comparison with the reanalysis result, it is useful to plot the instantaneous ψ_{PNA} and ψ_T fields during the life cycle of the model PNA event. For the parameter conditions given above, Fig. 10 shows the temporal evolution of the planetary-scale streamfunction anomaly ψ_{PNA} and total streamfunction ψ_T fields of an eddy-driven PNA$^-$ event in a weak background westerly wind (dashed line in Fig. 9a) with an initial amplitude of $B(x, y, 0) = 0.4\exp[-0.15(y - 0.75L_y)^2]e^{-\gamma_1 x^2}$ with $\gamma_1 = 0.005$. Figure 11 shows the life cycle of an eddy-driven PNA$^+$ event with $\gamma_1 = 0$ in a strong background westerly wind (solid line in Fig. 9a) for the parameters given above.

It is further found that the planetary-scale streamfunction anomaly ψ_{PNA} shows a quadrupole structure like a wave train structure, in which the dipole anomaly over the North Pacific has a more rapid growth than the downstream dipole probably due to the stronger forcing of preexisting eddy forcing at $x = -2.87/4$ during the PNA growing phase. Such a feature is more evident for the PNA$^+$ (Fig. 11a) than for the PNA$^-$ (Fig. 10a). It is also seen that the eddy-driven PNA anomaly has a lifetime or duration of about 15 days (10–20 days) due to the 2-week period forcing of preexisting eddy forcing $-\nabla\cdot(\mathbf{v}_1' q_1')_P$ (Luo et al. 2007), consistent with the reanalysis data. Furthermore, in the PNA anomaly ψ_{PNA} field the northern pole of the PNA is stronger than the southern pole, and this is due to the initial PNA dipole having a more intense northern pole than the southern pole. The model ψ_{PNA} field looks like the composite result from the reanalysis data shown in Fig. 3b. The total streamfunction field of the model PNA$^-$ (Fig. 10b) resembles the daily unfiltered Z500 field for the observed PNA$^-$ event (Fig. 1a), which corresponds to a large meandering of westerly jet streams or the presence of CWB. For the PNA$^+$, the obtained streamfunction anomaly ψ_{PNA} field is similar to the composite Z500 anomaly of PNA$^+$ events from the reanalysis data (Fig. 3a), whereas the model total streamfunction field ψ_T resembles the daily unfiltered Z500 field for a PNA$^+$ event (Fig. 1b), which corresponds to the absence of a large westerly jet meandering or CWB. Similar results are found for $L_y = 5$ (corresponding to 5000 km) (not shown).

In our model, we define the maximum value of the nondimensional streamfunction anomaly ψ_{PNA} in the north side of the channel as the intensity ψ_N of the PNA. Then we further define $D_I = (\psi_N - \psi_D)/\psi_N$ as the energy dispersion index of the PNA at every day, where ψ_D denotes the maximum intensity of the nondimensional streamfunction anomaly ψ_{PNA} of the northern pole of the downstream dipole in the east of $x = 0$. A high (low) D_I means weak (strong) dispersion for the PNA.

Figure 12 shows that the PNA anomaly moves westward for both of its two phases, with the PNA$^-$

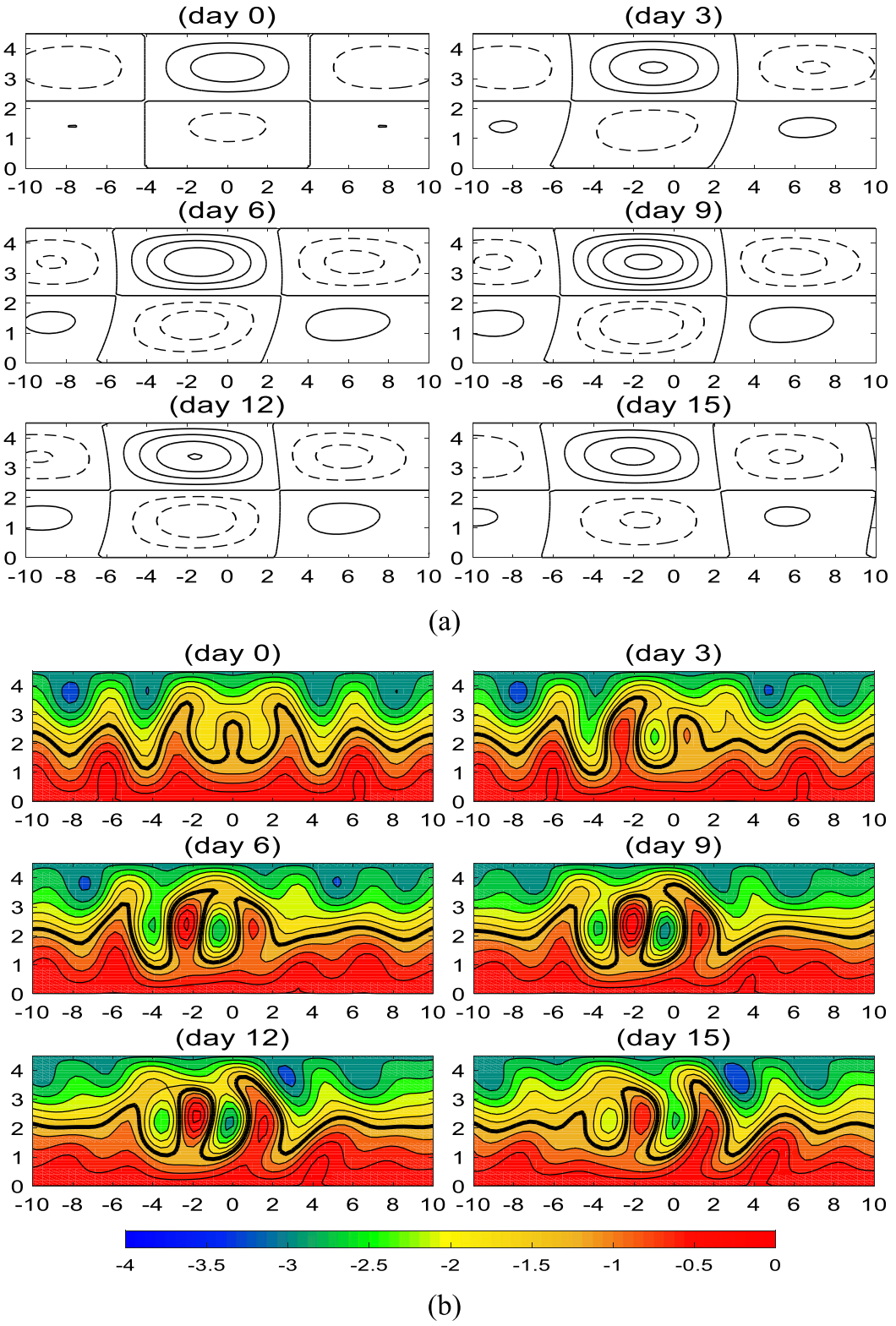

FIG. 10. Temporal evolutions of (a) planetary-scale anomaly streamfunction ψ_{PNA} (CI = 0.2) and (b) total streamfunction fields (CI = 0.3) for PNA^- event ($\alpha = -1$ and $m = -2\pi/L_y$) with the initial amplitude of $B(x, y, 0) = 0.4\exp[-\nu(y - 0.75L_y)^2]e^{-\gamma_1 x^2}$ for $\nu = 0.15$ and $\gamma_1 = 0.005$ under the forcing of preexisting synoptic-scale eddies with $\mu = 0.2$ and $x_T = 2.87/4$ from the extended UNMI model for given background zonal winds in Fig. 9. The thick solid line in (b) represents the contour line of -1.2, and the red (blue and green) shading represents the high (low) pressure region.

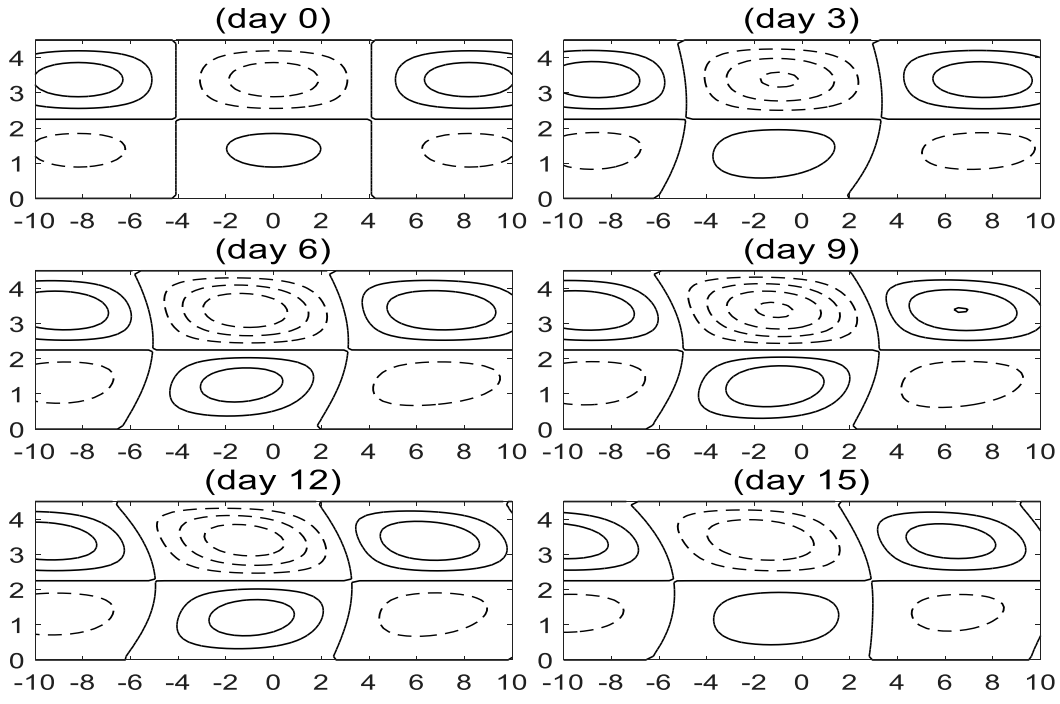

(a)

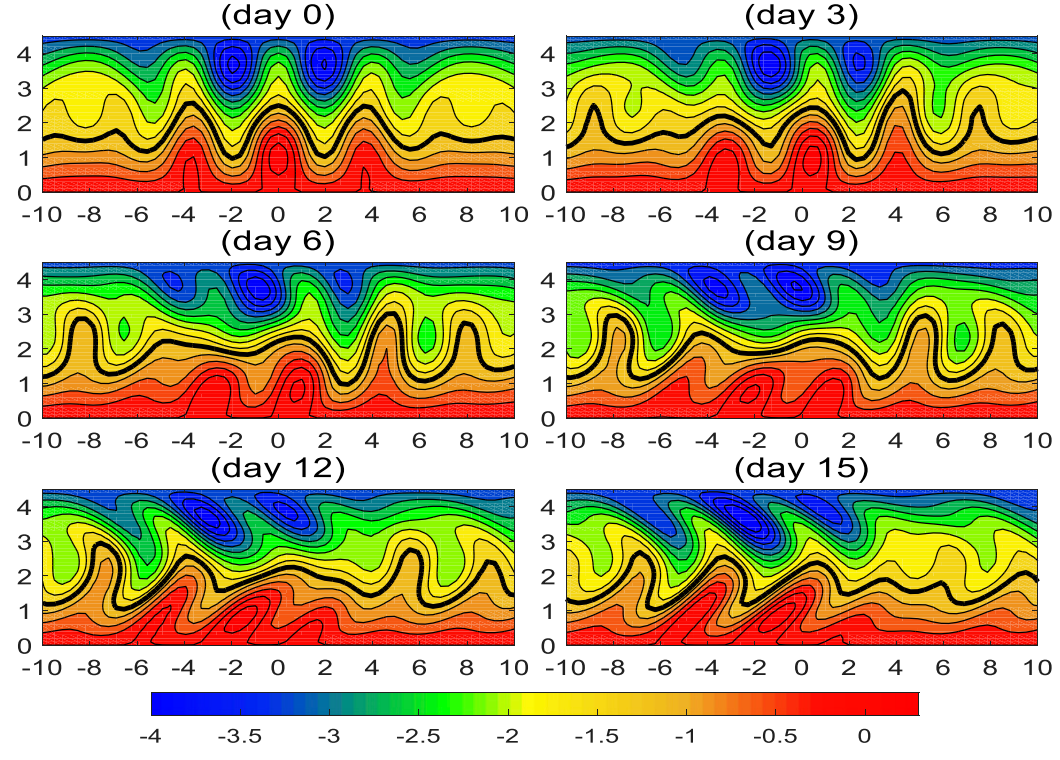

(b)

FIG. 11. As in Fig. 10, but for the PNA$^+$ event ($\alpha = 1$ and $m = 2\pi/L_y$) with initial amplitude of $B(x, y, 0) = 0.4\exp[-\nu(y - 0.75L_y)^2]e^{-\gamma_1 x^2}$ for $\nu = 0.15$ and $\gamma_1 = 0$.

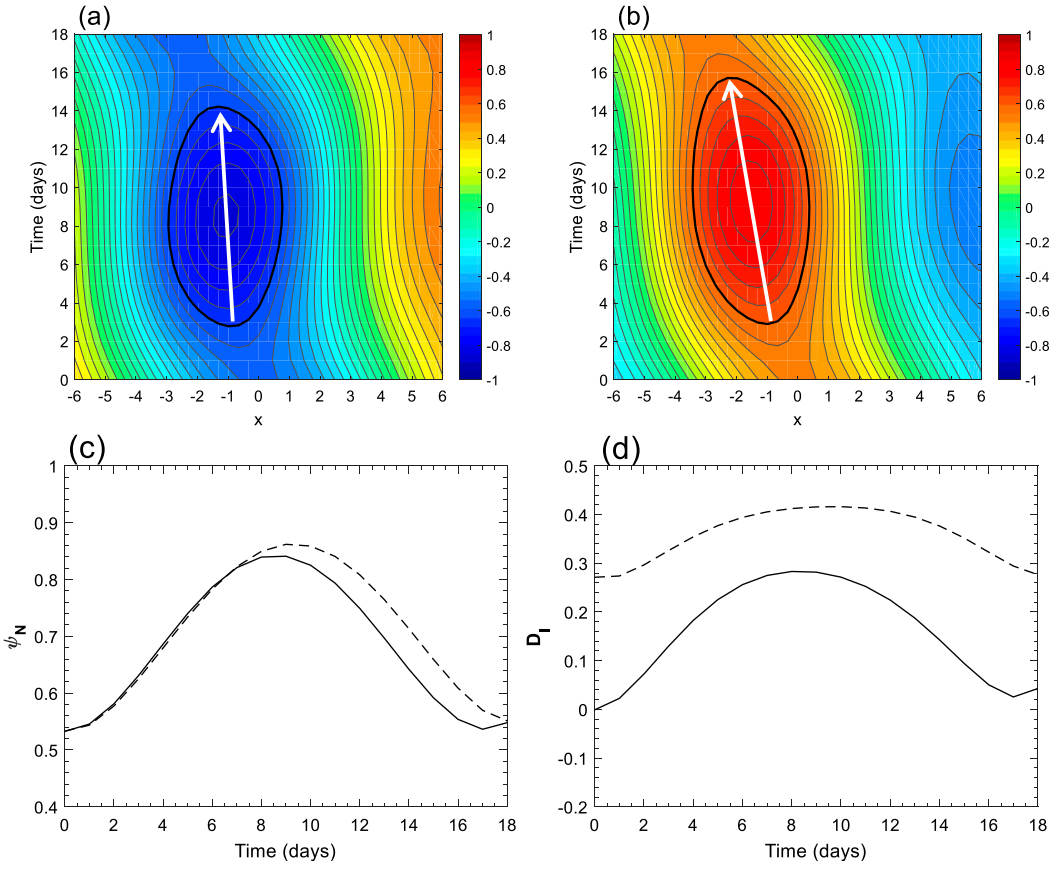

FIG. 12. (top) Time-zonal evolutions of PNA wave packet streamfunction anomaly ψ_{PNA} ($y = 0.75L_y$) for (a) PNA$^+$ (CI = 0.05; thick solid line is marked by the value of CI = −0.6) and (b) PNA$^-$ (CI = 0.05; thick solid line marked by the value of CI = 0.6) events obtained from the extended UNMI model for given background zonal winds in Fig. 9. (bottom) Time series of the daily (c) PNA intensity ψ_N and (d) energy dispersion index D_I for PNA$^+$ (solid line) and PNA$^-$ (dashed line) events for the initial PNA values of $B(x, y, 0) = 0.4\exp[-\nu(y - 0.75L_y)^2]e^{-\gamma_1 x^2}$ with $\gamma_1 = 0$ (solid line) and $\gamma_1 = 0.005$ (dashed line).

(Fig. 12b) moving westward faster than the PNA$^+$ (Fig. 12a). Moreover, the PNA$^-$ has a longer duration than the PNA$^+$, which is also seen from the temporal variation of the PNA intensity shown in Fig. 12c. These features are highly consistent with those seen in the reanalysis data (Fig. 2). The energy dispersion index D_I is always larger for the PNA$^-$ (dashed line in Fig. 12d) than for the PNA$^+$ (solid line in Fig. 12d), which suggests that the PNA$^+$ has a stronger energy dispersion than the PNA$^-$, in agreement with the reanalysis result (Fig. 4). This also means that the PNA$^+$ is more of a linear process than the PNA$^-$. Furthermore, the difference in the energy dispersion index D_I between the two phases is larger during its beginning and ending stages than its mature stage. Thus, the PNA tends to have the weakest energy dispersion during its mature phase, while the energy dispersion of the PNA$^+$ is stronger than that of the PNA$^-$. Such a time-varying feature of the energy dispersion is also quantitively consistent with the reanalysis data (Fig. 4). However, we note that the D_I peak is seen before the PNA mature stage in reanalysis (Fig. 4), but around the mature phase in the extended UNMI model. This D_I difference may be related to the exclusion of many factors such as baroclinicity (vertical wind shear and stratification), unstable synoptic-scale eddies and the eddy barotropic decay in the model. The PNA's duration becomes short and its intensity weakens when U_0 ($\sim$10 m s^{-1}) increases as shown in Table 2. The duration of the PNA is determined by the period of the eddy forcing in the form of $2\pi/\Delta\omega$ and $\Delta\omega \propto \mathrm{PV}_y$. Because $\mathrm{PV}_y = \beta - U_{yy} + FU$, the PNA duration is also influenced by the strength and meridional distribution of the background zonal wind U or the magnitude of PV$_y$. Furthermore, as γ_1 increases, the wave train structure of the PNA$^-$ becomes less distinct, but its duration and intensity do not change much.

The above results suggest that the differences in the background $U(y)$ and the associated PV$_y$ (Fig. 9), which

TABLE 2. Nondimensional maximum intensity and duration (days) of the PNA for corresponding parameters U_0 and γ_1 from the extended UNMI model for the background zonal wind of $U = U_0 + \Delta u(y - y_0)^2 e^{-\gamma(y-y_1)^2}$ and the initial amplitude of $B(x, y, 0) = 0.4\exp[-0.15(y - 0.75L_y)^2]e^{-\gamma_1 x^2}$, where $\Delta u = -0.07$, $\gamma = 0.05$, $y_0 = 2.5$, and $y_1 = 3.1$. Here, the daily intensity of the PNA is defined as the absolute value of the strongest streamfunction anomaly of the northern pole of the PNA at every day. The maximum intensity of the PNA is defined as the maximum value (peak day) of the daily intensity during the PNA life cycle. The duration of the PNA is defined as the number of days when the daily PNA intensity is above its threshold value of 0.6.

	γ_1			
U_0	0	0.002	0.004	0.006
	Nondimensional PNA intensity			
0.6	0.86	0.86	0.86	0.86
0.7	0.85	0.85	0.85	0.85
0.8	0.84	0.84	0.84	0.84
0.9	0.83	0.83	0.83	0.83
1.0	0.82	0.82	0.82	0.82
	Duration (days)			
0.6	14.6	14.4	14.3	14.4
0.7	13.1	13.2	13.2	13.3
0.8	12.3	12.4	12.4	12.5
0.9	11.9	11.9	11.8	11.9
1.0	11.4	11.4	11.5	11.4

resemble those in the reanalysis (Fig. 8), play a key role in producing the difference features of the PNA between its two phases. Specifically, because weaker (stronger) background $U(y)$ and PV_y are seen for the PNA^- (PNA^+), the lower (higher) PV_y regions corresponds to a domain with weaker (stronger) energy dispersion, stronger (weaker) nonlinearity and long-lived (short-lived) preexisting eddy forcing. Thus, the PNA^- can maintain its longer lifetime and larger amplitude than the PNA^+. Because $U(y)$ and PV_y are larger and the PNA^+ amplitude is smaller than those of the PNA^-, the westward movement of the PNA^+ is suppressed so that the PNA^+ has a slower westward movement than the PNA^-.

It is also useful to examine whether the above results depend on the parameter choice. We consider the same parameters as in Fig. 12, but vary the value of μ. The value of μ reflects the zonal distribution of the preexisting eddy forcing. For different values of μ, the time variation of the energy dispersion index D_I is shown in Fig. 13. It is seen that the zonally uniform preexisting eddy forcing ($\mu = 0$) can enhance the energy dispersion of the PNA even during the mature stage (Fig. 13a). Such an eddy forcing shape does not take place over the North Pacific because the North Pacific storm track is often zonally localized. We also find that the duration and strength of the PNA depend on the value of μ rather than the value of x_T (not shown). Especially, the PNA is slightly intensified and its duration is slightly shortened as μ increases for $\mu > 0$. The variation of D_I shows that the energy dispersion of the PNA tends to weaken as it intensifies, but strengthen after the PNA peak, even though the PNA^+ has stronger energy dispersion than the PNA^- (Figs. 13c,d). In this situation, the time variation of the energy dispersion index D_I of the PNA is in good agreement with that of the reanalysis data (Fig. 4). Thus, only when the PNA is excited by the localized synoptic-scale eddies over the North Pacific, the obtained theoretical result is more consistent with the observation.

Here, we further consider the impact of the zonal position of the preexisting eddy forcing on the energy dispersion of the PNA. For the same condition as in Figs. 10 and 11, the temporal variation of the daily energy dispersion index D_I is shown in Fig. 14 for $\mu = 0.2$ and different values of x_T. It is noted that when the preexisting eddy forcing is moved to the position of the initial PNA, the energy dispersion of eddy-driven PNA tends to be intensified because D_I becomes small, even when it is located on the downstream side of the initial PNA^+ (Figs. 14c,d). Thus, the zonal position of upstream synoptic-scale eddies can also influence the energy dispersion or wave train structure of the PNA (Figs. 14a–d).

d. *Effect of the initial PNA$^-$ distribution*

To quantify the effect of the initial structure of the PNA on its energy dispersion, it is useful to suppose that the spatial distribution of the initial PNA^+ (PNA^-) has the form of $B(x, y, 0) = 0.4\exp[-0.15(y - 0.75L_y)^2]$ ($B(x, y, 0) = 0.4\exp[-0.15(y - 0.75L_y)^2]e^{-\gamma_1 x^2}$ for $\gamma_1 > 0$). Here, we fix the initial condition of the PNA^+, but vary the value of γ_1 in the initial PNA^- distribution. The time variation of the daily energy dispersion index D_I of the PNA^- and PNA^+ is shown in Fig. 15 for $\gamma_1 = 0$, $\gamma_1 = 0.002$, $\gamma_1 = 0.004$, and $\gamma_1 = 0.006$ with $\mu = 0.2$ and $x_T = 2.87/4$. As seen from Fig. 15, the D_I value of the PNA^- increases as γ_1 increases. This means that the energy dispersion of the PNA^- can be reduced (dashed line in Figs. 15a–d), when its initial amplitude has an increased zonal locality. Thus, the weaker energy dispersion of the PNA^- is also related to the stronger zonal locality of the initial PNA^- than the PNA^+. We also note that the PNA^+ has a stronger energy dispersion than the PNA^- only during the decaying phase when they have the same initial value (not shown). A similar result is also found for the NAO case (Fig. 4 of Luo et al. 2018) because the observed NAO^- and NAO^+ have almost the same initial zonal distributions (not shown).

We further examine the effect of the increased difference of the initial PNA between its two phases on the PNA asymmetry in energy dispersion. For the same background wind in the form of $U = U_0 + \Delta u(y - y_0)^2 e^{-\gamma(y-y_1)^2}$

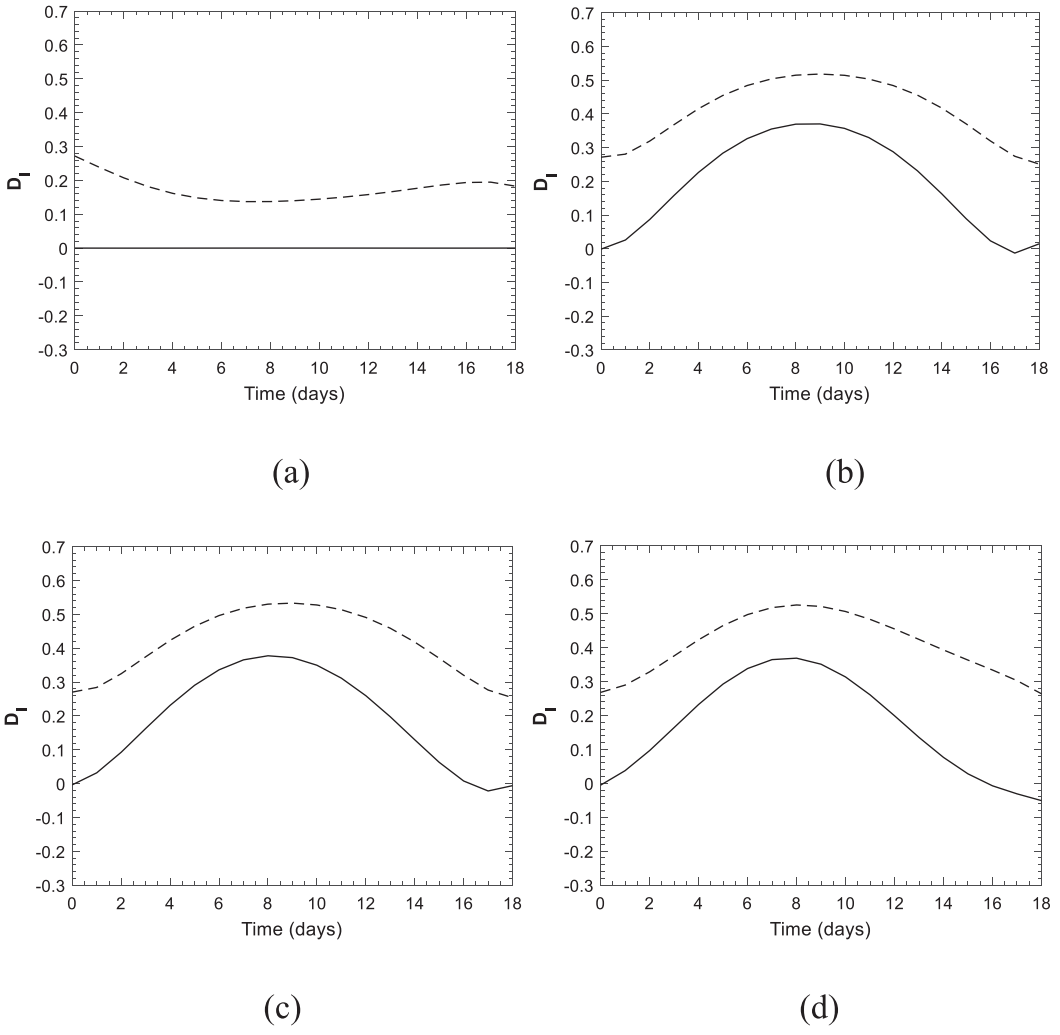

FIG. 13. Time variations of daily energy dispersion index D_I of PNA$^+$ and PNA$^-$ events with the initial conditions of $B(x, y, 0) = 0.4\exp[-0.15(y - 0.75L_y)^2]e^{-\gamma_1 x^2}$ for $\gamma_1 = 0$ (PNA$^+$; solid line) and $\gamma_1 = 0.005$ (PNA$^-$; dashed line) cases during the PNA life cycle for (a) $\mu = 0$, (b) $\mu = 0.5$, (c) $\mu = 1.0$, and (d) $\mu = 1.5$ with $x_T = 2.87/4$ and the same parameters as in Table 1 obtained from the extended UNMI model for given background zonal winds in Fig. 9.

($U_0 = 0.8, \Delta u = -0.07, \gamma = 0.05, y_0 = 2.5$, and $y_1 = 3.1$), we show the temporal variation of the daily energy dispersion index D_I of the PNA$^-$ and PNA$^+$ in Fig. 16 for $\gamma_1 = 0$, $\gamma_1 = 0.002$, $\gamma_1 = 0.004$, and $\gamma_1 = 0.006$ with $\mu = 0.2$ and $x_T = 2.87/4$, when $B(x, y, 0) = 0.4\exp[-0.15(y - 0.75L_y)^2]e^{-\gamma_1 x^2}$ is considered as the initial value of the PNA$^+$ ($\gamma_1 = 0$) and PNA$^-$ ($\gamma_1 \neq 0$). Here, the difference of the initial PNA between its two phases is increased when the positive value of γ_1 increases. It is seen from Fig. 16 that there is no difference of the energy dispersion between both phases of the PNA if the same initial PNA amplitude ($\gamma_1 = 0$) and same background westerly wind $U(y)$ are considered. The difference of the energy dispersion between the two phases of the PNA is increased as the initial PNA difference (γ_1) increases (Figs. 16b–d). However, we note that the initial PNA difference has a larger impact on the energy dispersion difference of the PNA between its two phases during the earlier stage of the PNA than during its decaying phase. Such an effect is also evident during the decaying phase (Figs. 15b–d) when a background $U(y)$ difference is included in the UNMI model. Thus, when both the initial PNA and background $U(y)$ differences are considered, the temporal evolution of the obtained model energy dispersion index is more consistent with the reanalysis result (Fig. 4). The analytical solution of Eq. (2h) without forcing reveals that when the background PV$_y$ is smaller (larger), the initial PNA has a more (less) zonally localized distribution for the PNA$^-$ (PNA$^+$). Thus, a less (more)

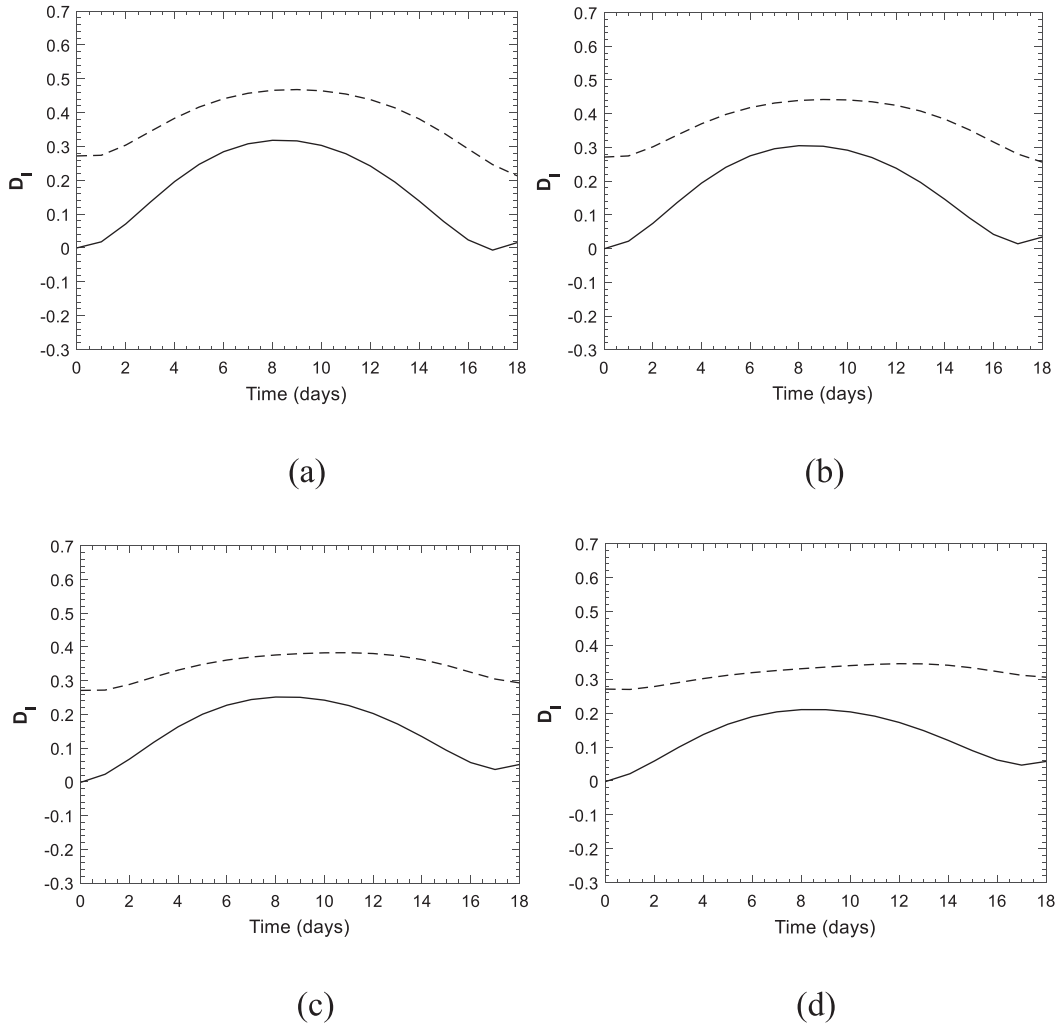

FIG. 14. Time variations of daily energy dispersion index D_I of the PNA$^+$ and PNA$^-$ events with the initial conditions of $B(x, y, 0) = 0.4\exp[-0.15(y - 0.75L_y)^2]e^{-\gamma_1 x^2}$ for $\gamma_1 = 0$ (PNA$^+$; solid line) and $\gamma_1 = 0.005$ (PNA$^-$; dashed line) cases during the PNA life cycle for (a) $x_T = 2.87$, (b) $x_T = 2.87/2$, (c) $x_T = 0$, and (d) $x_T = -2.87/4$ with $\mu = 0.2$ and the same parameters as in Table 1 obtained from the extended UNMI model for given background zonal winds in Fig. 9.

zonally localized structure of the initial PNA$^+$ (PNA$^-$) is, to some extent, related to the larger (smaller) background PV$_y$ over the North Pacific. This suggests that the background $U(y)$ or PV$_y$ difference over the North Pacific is likely the most key factor for determining the PNA asymmetry between its two phases through its influence on the initial PNA structure and the subsequent movement and energy dispersion of the amplified PNA. As a result, we can conclude from the above results that the main features of the PNA in the reanalysis data can be better captured by our extended UNMI model.

6. A comparison between the PNA and NAO

In this section, it is useful to estimate the nondimensional nonlinear phase speeds of the PNA and NAO using the reanalysis data from Eq. (3) to further explain the difference of the zonal movement between the PNA and NAO anomalies. In fact, because Eq. (3) is derived based on the barotropic atmosphere assumption, it is difficult to exactly determine the zonal movement speeds of observed PNA and NAO. Considering the large difference of background $U(y)$ between two phases of the PNA over the latitude band (25°–45°N) and the center of the northern pole being located on 45°–50°N, the nondimensional U and PV$_y$ in Eq. (3) are obtained by calculating U500 and PV$_y = \beta - (\mathrm{U500})_{yy} + F \times (\mathrm{U500})$ averaged over the region 35°–60°N, 160°E–140°W for the PNA. Similarly, considering the large difference of background $U(y)$ between two phases of the NAO over the latitude band 45°–65°N and the center of the northern pole being located on 65°N, $U(y)$ and

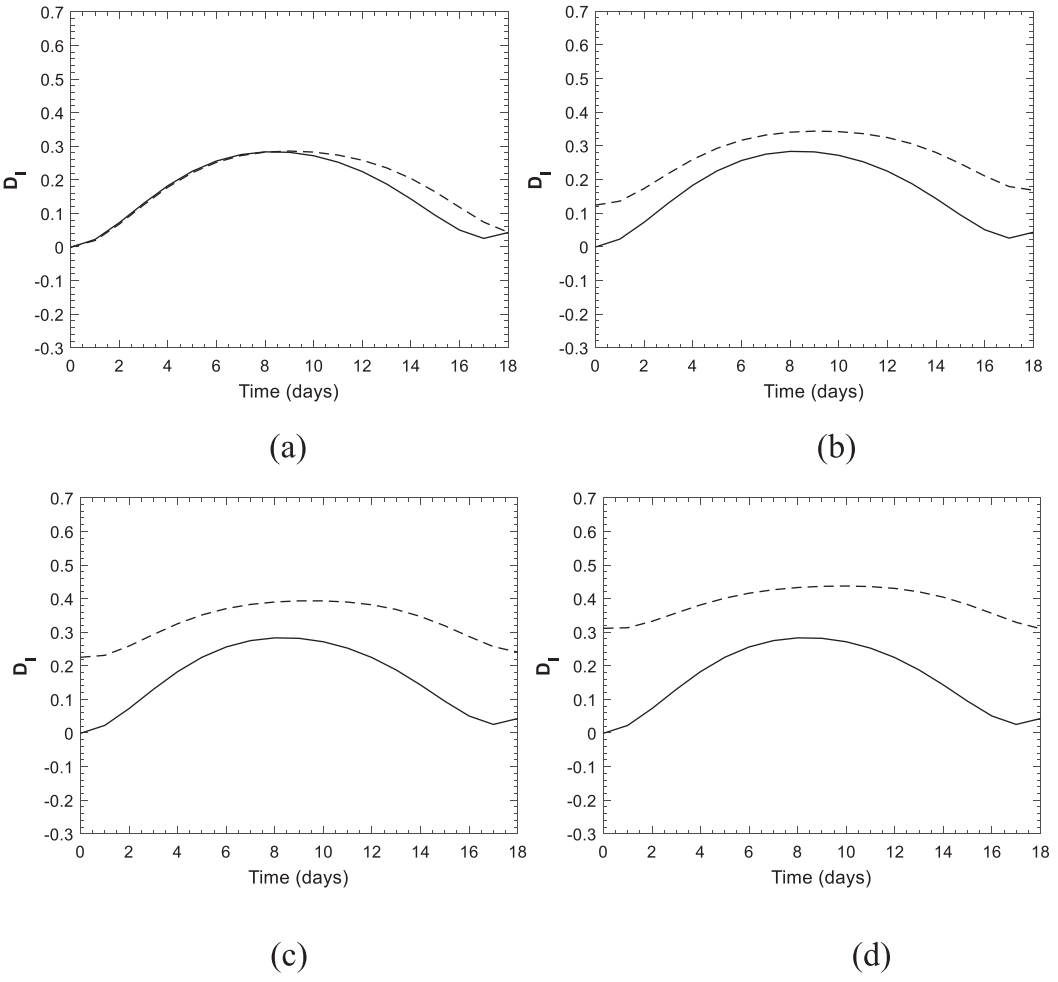

FIG. 15. Time variations of daily energy dispersion index D_I of the PNA$^+$ (solid line) with the initial value of $B(x, y, 0) = 0.4\exp[-0.15(y - 0.75L_y)^2]$ and PNA$^-$ (dashed line) with the initial value of $B(x, y, 0) = 0.4\exp[-0.15(y - 0.75L_y)^2]e^{-\gamma_1 x^2}$ during the PNA life cycle for (a) $\gamma_1 = 0$, (b) $\gamma_1 = 0.002$, (c) $\gamma_1 = 0.004$, and (d) $\gamma_1 = 0.006$ with $\mu = 0.2$, $x_T = 2.87/4$, and the same parameters as in Table 1 obtained from the extended UNMI model for given background zonal winds in Fig. 9.

PV_y are calculated over the region 45°–70°N, 70°W–20°E for the NAO. We calculate the domain average of nondimensional daily Z500 anomaly over the region 40°–50°N, 170°E–160°W or 60°–70°N, 60°–20°W as the daily M_0 of the PNA or NAO in terms of Eq. (2c).

Using the parameters $k = 2/(6.371\cos\varphi_0)$, $m = \pm 2\pi/L_y$, and the nondimensional β on the reference latitude φ_0, the daily nonlinear phase speed of the PNA$^-$ (PNA$^+$) and NAO$^+$ (NAO$^-$) can be estimated from Eq. (3). For $L_y = 5$ (corresponding to a meridional scale of 5000 km), we choose $\varphi_0 = 45$°N ($\varphi_0 = 65$°N) as the meridional position of the northern pole of the PNA (NAO) dipole to estimate the nonlinear phase speed of the PNA (NAO).

We show the nondimensional nonlinear phase speeds of the composite daily PNA and NAO anomalies in Fig. 17 for individual PNA and NAO events given in section 3. It is interesting to note that the PNA$^+$ and PNA$^-$ move westward (Fig. 17a) and their westward speeds increase with the increased amplitude, in which the westward speed of the PNA$^-$ is about 2 times than of the PNA$^+$ during the PNA mature phase (from lag −2 to 2 days). The main cause of this difference is that the PNA$^-$ has larger amplitude and smaller background PV_y than the PNA$^+$ so that $-\delta_N M_0^2/(2k\mathrm{PV}_y)$ in C_{NP} becomes much more important than the mean zonal wind-induced eastward speed. In this case, the large westward movement of the PNA$^-$ is inevitably seen. However, we see from Fig. 17b that the NAO$^+$ (NAO$^-$) anomaly shows an eastward (westward) movement during the NAO growing phase. The eastward (westward) speed of the NAO$^+$ (NAO$^-$) increases weakly (strongly) with the increased amplitude, in which the westward movement

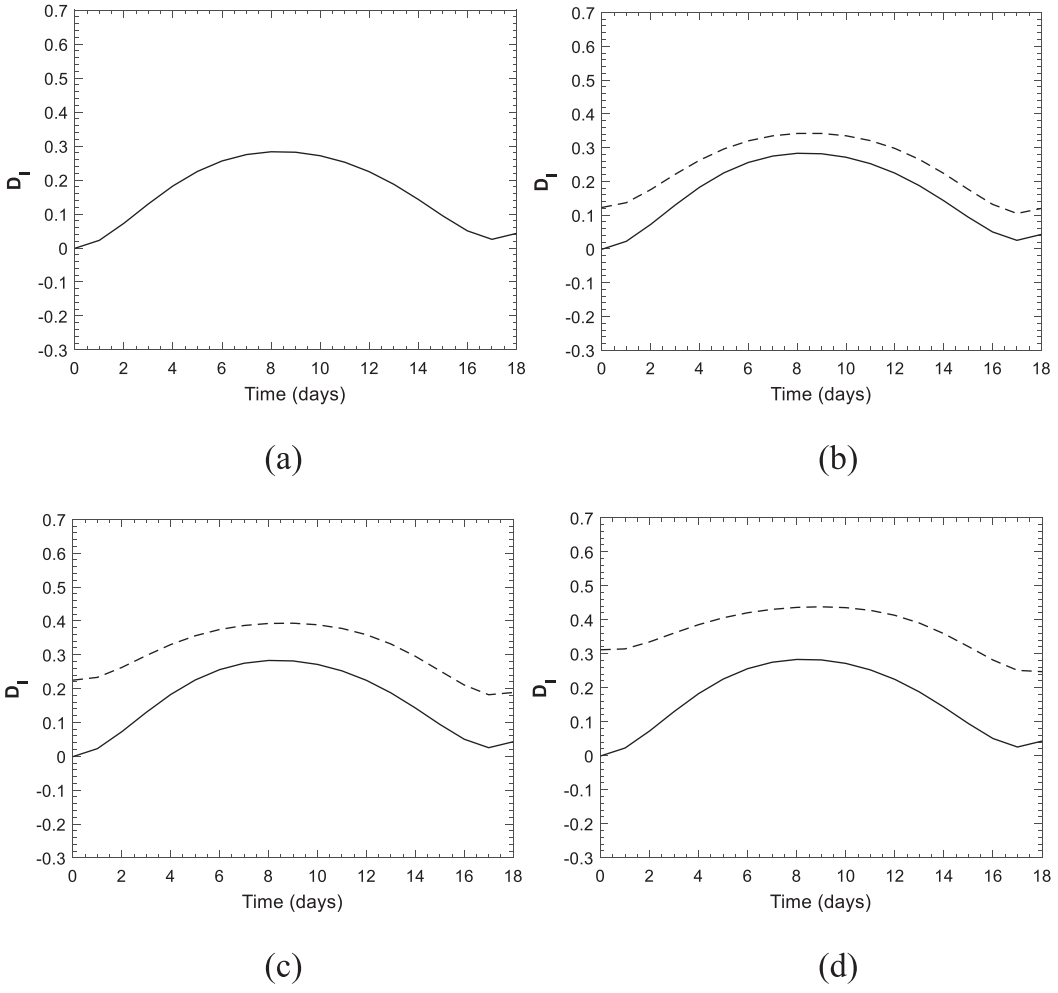

FIG. 16. Time variations of daily energy dispersion index D_I of the PNA$^+$ (solid line) with the initial value of $B(x, y, 0) = 0.4\exp[-0.15(y - 0.75L_y)^2]$ and PNA$^-$ (dashed line) with the initial value of $B(x, y, 0) = 0.4\exp[-0.15(y - 0.75L_y)^2]e^{-\gamma_1 x^2}$ during the PNA life cycle in the same basic zonal wind of $U = U_0 + \Delta u(y - y_0)^2 e^{-\gamma(y-y_1)^2}$ ($U_0 = 0.8$, $\Delta u = -0.07$, $\gamma = 0.05$, $y_0 = 2.5$, and $y_1 = 3.1$) obtained from the extended UNMI model for (a) $\gamma_1 = 0$, (b) $\gamma_1 = 0.002$, (c) $\gamma_1 = 0.004$, and (d) $\gamma_1 = 0.006$ with $\mu = 0.2$ and $x_T = 2.87/4$.

of the NAO$^-$ is more intense than the eastward movement of the NAO$^+$. In this case, it is concluded that the PNA has zonal movements different from those of the NAO. Nevertheless, the physical cause of why the NAO$^+$ (NAO$^-$) undergoes eastward (westward) movement has been investigated in Luo et al. (2018); thus, it is not further discussed here. For a comparison, it is also useful to estimate the time-mean nonlinear phase speed of the PNA and NAO from Fig. 17. The time-mean nonlinear phase speed averaged from lag −4 to 4 in Fig. 17a in a dimensional unit is about −2.4 (−1.0) m s^{-1} for the PNA$^-$ (PNA$^+$), whereas its corresponding dimensional time-mean phase speed is −3.8 (2.8) m s^{-1} for the NAO$^-$ (NAO$^+$). These estimated speeds are basically consistent with the above results from the reanalysis data, although slightly low. Thus, the movement features of the PNA and NAO anomaly obtained for the reanalysis data presented in section 3 can be better explained by the theoretical results from the extended UNMI model.

7. Conclusions and discussion

In this paper, we have first analyzed the PNA$^-$ and PNA$^+$ events occurring over the North Pacific in winter from 1950 to 2017 using NCEP–NCAR reanalysis data. It is found that the PNA$^-$ (PNA$^+$) events are associated with strong (weak) cyclonic wave breaking (CWB) or large (small) meandering of a westerly jet stream over the North Pacific and North America. The reanalysis composite results reveal that while both phases of the PNA show a quadrupole structure composed of a wave train structure, its negative phase (PNA$^-$) has a larger

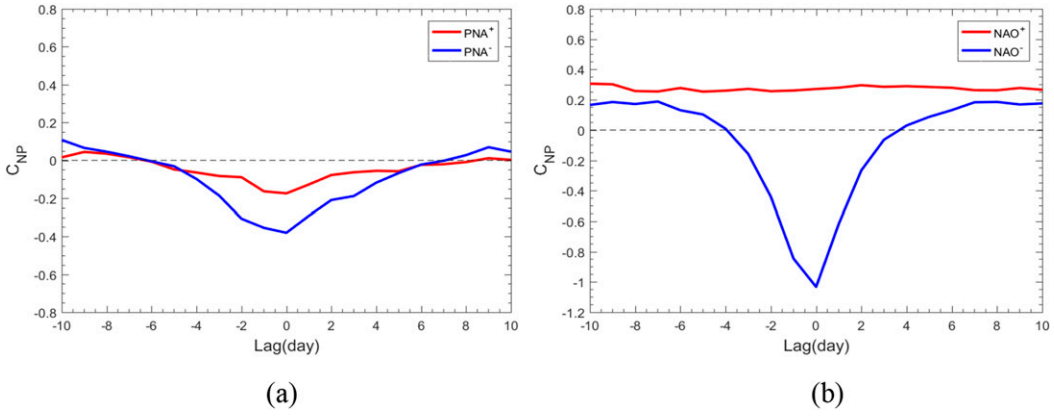

FIG. 17. Time variations of nondimensional daily nonlinear phase speed C_{NP} from lag −10 to 10 days for (a) PNA^+ (red line) and PNA^- (blue line) and (b) NAO^+ (red line) and NAO^- (blue line) events identified from the reanalysis data. Here, the nondimensional U and PV_y are obtained by calculating the domain averages of U500 and associated PV_y over the region 35°–60°N, 160°E–140°W for the PNA or over the region 45°–70°N, 70°W–20°E for the NAO. The nondimensional M_0 is obtained by calculating the domain average of daily Z500 anomaly over the region 40°–50°N, 170°W–160°E for the PNA or over the region 60°–70°N, 60°–20°W for the NAO.

amplitude and longer lifetime than its positive phase (PNA^+). Both PNA^- and PNA^+ events exhibit westward movements, but the speed of the PNA^- is about twice that of the PNA^+. Thus, the PNA shows a distinct asymmetry between its two phases. Furthermore, the PNA differs from the NAO in the North Atlantic in that the positive phase NAO (NAO^+) moves eastward whereas its negative phase (NAO^-) moves westward, in contrast to the PNA, which moves westward for both phases.

We then modified and applied a theoretical model, namely the unified nonlinear multiscale interaction (UNMI) model previously applied to the NAO by Luo et al. (2018), to reveal the physical cause of the PNA asymmetry between its two phases. The model results suggest that the eddy-driven dipole over the North Pacific can have strong energy dispersion and weak nonlinearity (compared with the NAO) because of the strong meridional background PV gradient (PV_y) resulting from its lower-latitude location. Such a strong energy dispersion can lead to the generation of a strong quadrupole structure that forms a wave train pattern like the PNA, whereas the weak energy dispersion during NAO events would result in a weak wave train structure. Because of its weak nonlinearity and strong energy dispersion in comparison with the NAO, the PNA is predominantly a linear process, even though it is considered as a nonlinear initial-value problem. In contrast, the NAO anomaly behaves as a nonlinear process because of its small PV_y, which leads to strong nonlinearity and weak energy dispersion. Furthermore, the PNA^- is shown to have weaker energy dispersion and stronger nonlinearity than the PNA^+ because the background zonal wind and PV_y prior to the onset of the PNA^- are weaker than those for the PNA^+. The weaker energy dispersion leads to a larger amplitude, longer lifetime and more rapid westward movement for the PNA^- than the PNA^+. Previous studies (e.g., Feldstein 2002; Mori and Watanabe 2008) cannot provide these explanations, although their diagnostic results showed that the PNA life cycle is a strongly linear process, which is confirmed and explained by our theoretical results. Because the energy dispersion and nonlinearity of the PNA are directly related to the magnitude of the background PV_y in the extended UNMI model, the meridional distribution and strength of the background zonal wind over the North Pacific, rather than the zonal inhomogeneity of the background zonal wind, determine the PV_y and thus are crucial for the linear evolution of the PNA.

Moreover, the energy dispersion is much stronger for the PNA^+ than the PNA^- during their growing and decaying phases in the extended UNMI model (although the difference is small during the disappearance phase in the reanalysis), but the difference is small during their mature phase. This feature is different from that of the NAO, which shows stronger energy dispersion and weaker nonlinearity during the NAO^+ than the NAO^- only during the decaying phase. Again, such an energy dispersion difference between the two phases is related to the initial structures of the PNA^+ and PNA^-. Specifically, the initial PNA^+ (PNA^-) possesses a less (more) zonally localized structure presumably related to its large (small) PV_y prior to their onset, this leads to relatively strong (weak) energy dispersion for the amplified PNA^+ (PNA^-) after the onset. While the background zonal wind and PV_y differences mainly cause the PNA asymmetry during the decaying phase, the initial

structure difference leads to enhanced asymmetry of the PNA during the growing and decaying phases. Thus, the asymmetry of the PNA between its two phases is related to the weak (strong) zonal variations in the initial field for the PNA^+ (PNA^-).

The extended UNMI model and the initial U and PV_y conditions are based on a barotropic atmosphere. Whether the model results hold for a baroclinic atmosphere is not examined in this paper. Also, what physical process determines the difference in the initial PNA and background conditions between its two phases is not addressed in this paper. Furthermore, it is unclear whether our extended UNMI model can be applied to investigate recent cases with variant PNA modes, for example, such as that leading to the 2013/14 drought in California (Singh et al. 2016; S.-Y. Wang et al. 2017; Swain et al. 2018). These issues deserve further investigations.

Acknowledgments. The authors acknowledge the support from the National Natural Science Foundation of China (Grants 41490642 and 4143000305) and the National Key Research and Development Program of China (2016YFA0601802). Dai acknowledges the funding support from the U.S. National Science Foundation (Grant OISE-1743738) and the U.S. National Oceanic and Atmospheric Administration (Award NA18OAR4310425).

APPENDIX

Coefficients of the Analytical Solution [Eq. (2)] for the Extended UNMI Model

The following equations define the coefficients in Eqs. (2d)–(2h) for the extended UNMI model:

$$p_j = \frac{(k-2\tilde{k}_j)}{\mathrm{PV}_y\left\{\tilde{k}_j + k - \left(\frac{\tilde{k}_j}{\tilde{k}_j^2 + m^2/4 + F} + \frac{k}{k^2+m^2+F}\right)[(\tilde{k}_j+k)^2 + 9m^2/4 + F]\right\}},$$

$$r_j = \frac{(k+2\tilde{k}_j)}{\mathrm{PV}_y\left\{\tilde{k}_j + k - \left(\frac{\tilde{k}_j}{\tilde{k}_j^2 + m^2/4 + F} + \frac{k}{k^2+m^2+F}\right)[(\tilde{k}_j+k)^2 + m^2/4 + F]\right\}},$$

$$s_j = \frac{(k+2\tilde{k}_j)}{\mathrm{PV}_y\left\{\tilde{k}_j - k - \left(\frac{\tilde{k}_j}{\tilde{k}_j^2 + m^2/4 + F} - \frac{k}{k^2+m^2+F}\right)[(\tilde{k}_j-k)^2 + 9m^2/4 + F]\right\}},$$

$$h_j = \frac{(k-2\tilde{k}_j)}{\mathrm{PV}_y\left\{\tilde{k}_j - k - \left(\frac{\tilde{k}_j}{\tilde{k}_j^2 + m^2/4 + F} - \frac{k}{k^2+m^2+F}\right)[(\tilde{k}_j-k)^2 + m^2/4 + F]\right\}},$$

$$q_{Nn} = \frac{4k^2 m}{L_y\{1-(m^2+F-k^2)[F+m^2(n+1/2)^2]/(k^2+m^2+F)^2\}}$$

$$Q_j = k^2 + m^2 - (\tilde{k}_j^2 + m^2/4), \quad (j=1,2),$$

$$\delta_N = \frac{km\sum_{n=1}^{\infty} q_{Nn} g_n^2 [k^2+m^2-m^2(n+1/2)^2]}{k^2+m^2+F},$$

$$g_n = \frac{8}{m[4-(n+1/2)^2]L_y},$$

$$G = \alpha\sqrt{\frac{L_y}{2}}\frac{(\tilde{k}_1+\tilde{k}_2)^2(\tilde{k}_2-\tilde{k}_1)m}{4(k^2+m^2+F)}, \quad \alpha = \pm 1.$$

REFERENCES

Barnston, A. G., and R. E. Livezey, 1987: Classification, seasonality, and persistence of low-frequency atmospheric circulation patterns. *Mon. Wea. Rev.*, **115**, 1083–1126, https://doi.org/10.1175/1520-0493(1987)115<1083:CSAPOL>2.0.CO;2.

Baxter, S., and S. Nigam, 2013: The subseasonal teleconnection analysis: PNA development and its relationship to the NAO. *J. Climate*, **26**, 6733–6741, https://doi.org/10.1175/JCLI-D-12-00426.1.

Berggren, R., B. Bolin, and C.-G. Rossby, 1949: An aerological study of zonal motion, its perturbations and break-down. *Tellus*, **1** (2), 14–37, https://doi.org/10.3402/tellusa.v1i2.8501.

Branstator, G., 1992: The maintenance of low-frequency atmospheric anomalies. *J. Atmos. Sci.*, **49**, 1924–1945, https://doi.org/10.1175/1520-0469(1992)049<1924:TMOLFA>2.0.CO;2.

Cash, B., and S. Lee, 2001: Observed nonmodal growth of the Pacific–North American teleconnection pattern. *J. Climate*, **14**, 1017–1028, https://doi.org/10.1175/1520-0442(2001)014<1017:ONGOTP>2.0.CO;2.

Dickson, R. R., and J. Namias, 1976: North American influence on the circulation and climate of the North Atlantic sector. *Mon. Wea. Rev.*, **104**, 1255–1265, https://doi.org/10.1175/1520-0493(1976)104<1255:NAIOTC>2.0.CO;2.

Feldstein, S. B., 2002: Fundamental mechanisms of the growth and decay of the PNA teleconnection pattern. *Quart. J. Roy. Meteor. Soc.*, **128**, 775–796, https://doi.org/10.1256/0035900021643683.

Franzke, C., and S. B. Feldstein, 2005: The continuum and dynamics of Northern Hemisphere teleconnection patterns. *J. Atmos. Sci.*, **62**, 3250–3267, https://doi.org/10.1175/JAS3536.1.

——, ——, and S. Lee, 2011: Synoptic analysis of the Pacific–North American teleconnection pattern. *Quart. J. Roy. Meteor. Soc.*, **137**, 329–346, https://doi.org/10.1002/qj.768.

Frederiksen, J., 1983: A unified three-dimensional instability theory of the onset of blocking and cyclogenesis. II: Teleconnection patterns. *J. Atmos. Sci.*, **40**, 2593–2609, https://doi.org/10.1175/1520-0469(1983)040<2593:AUTDIT>2.0.CO;2.

Harnik, N., G. Messori, R. Caballero, and S. B. Feldstein, 2016: The circumglobal North American wave pattern and its relation to cold events in eastern North America. *Geophys. Res. Lett.*, **43**, 11 015–11 023, https://doi.org/10.1002/2016GL070760.

Horel, J. D., and J. M. Wallace, 1981: Planetary-scale atmospheric phenomena associated with the Southern Oscillation. *Mon. Wea. Rev.*, **109**, 813–829, https://doi.org/10.1175/1520-0493(1981)109<0813:PSAPAW>2.0.CO;2.

Hoskins, B. J., and D. Karoly, 1981: The steady linear response of a spherical atmosphere to thermal and orographic forcing. *J. Atmos. Sci.*, **38**, 1179–1196, https://doi.org/10.1175/1520-0469(1981)038<1179:TSLROA>2.0.CO;2.

Kalnay, E., and Coauthors, 1996: The NCEP/NCAR 40-Year Reanalysis Project. *Bull. Amer. Meteor. Soc.*, **77**, 437–471, https://doi.org/10.1175/1520-0477(1996)077<0437:TNYRP>2.0.CO;2.

Lau, N.-C., 1988: Variability of the observed midlatitude storm tracks in relation to low-frequency changes in the circulation pattern. *J. Atmos. Sci.*, **45**, 2718–2743, https://doi.org/10.1175/1520-0469(1988)045<2718:VOTOMS>2.0.CO;2.

——, and M. J. Nath, 1991: Variability of the baroclinic and barotropic transient eddy forcing associated with monthly changes in the midlatitude storm tracks. *J. Atmos. Sci.*, **48**, 2589–2613, https://doi.org/10.1175/1520-0469(1991)048<2589:VOTBAB>2.0.CO;2.

Luo, D., 2000: Planetary-scale baroclinic envelope Rossby solitons in a two-layer model and their interaction with synoptic-scale eddies. *Dyn. Atmos. Oceans*, **32**, 27–74, https://doi.org/10.1016/S0377-0265(99)00018-4.

——, 2005: A barotropic envelope Rossby soliton model for block–eddy interaction. Part I: Effect of topography. *J. Atmos. Sci.*, **62**, 5–21, https://doi.org/10.1175/1186.1.

——, and J. Li, 2000: Barotropic interaction between planetary- and synoptic-scale waves during the life cycle of blockings. *Adv. Atmos. Sci.*, **17**, 649–670, https://doi.org/10.1007/s00376-000-0026-5.

——, F. Huang, and Y. Diao, 2001: Interaction between antecedent planetary-scale envelope soliton blocking anticyclone and synoptic-scale eddies: Observations and theory. *J. Geophys. Res.*, **106**, 31 795–31 815, https://doi.org/10.1029/2000JD000086.

——, A. Lupo, and H. Wan, 2007: Dynamics of eddy-driven low-frequency dipole modes. Part I: A simple model of North Atlantic Oscillations. *J. Atmos. Sci.*, **64**, 3–28, https://doi.org/10.1175/JAS3818.1.

——, J. Cha, L. Zhong, and A. Dai, 2014: A nonlinear multiscale interaction model for atmospheric blocking: The eddy-blocking matching mechanism. *Quart. J. Roy. Meteor. Soc.*, **140**, 1785–1808, https://doi.org/10.1002/qj.2337.

——, L. Zhong, and C. Franzke, 2015: Inverse energy cascades in an eddy-induced NAO-type flow: Scale interaction mechanism. *J. Atmos. Sci.*, **72**, 3417–3448, https://doi.org/10.1175/JAS-D-15-0062.1.

——, X. Chen, and S. Feldstein, 2018: Linear and nonlinear dynamics of North Atlantic Oscillations: A new thinking of symmetry breaking. *J. Atmos. Sci.*, **75**, 1955–1977, https://doi.org/10.1175/JAS-D-17-0274.1.

——, W. Zhang, L. Zhong, and A. Dai, 2019: A nonlinear theory of atmospheric blocking: A potential vorticity gradient view. *J. Atmos. Sci.*, **76**, 2399–2427, https://doi.org/10.1175/JAS-D-18-0324.1.

Mori, M., and M. Watanabe, 2008: The growth and triggering mechanisms of the PNA: A MJO-PNA coherence. *J. Meteor. Soc. Japan*, **86**, 213–236, https://doi.org/10.2151/jmsj.86.213.

Muslu, G. M., and H. A. Erbay, 2005: Higher-order split-step Fourier schemes for the generalized nonlinear Schrödinger equation. *Math. Comput. Simul.*, **67**, 581–595, https://doi.org/10.1016/j.matcom.2004.08.002.

Schulte, J. A., and S. Lee, 2017: Strengthening North Pacific influences on United States temperature variability. *Sci. Rep.*, **7**, 124, https://doi.org/10.1038/s41598-017-00175-y.

Singh, D., D. L. Swain, J. S. Mankin, D. E. Horton, L. N. Thomas, B. Rajaratnam, and N. S. Diffenbaugh, 2016: Recent amplification of the North American winter temperature dipole. *J. Geophys. Res. Atmos.*, **121**, 9911–9928, https://doi.org/10.1002/2016JD025116.

Song, J., 2018: Understanding anomalous synoptic eddy vorticity forcing in Pacific–North American teleconnection pattern events. *J. Atmos. Sci.*, **75**, 4287–4312, https://doi.org/10.1175/JAS-D-18-0071.1.

Swain, D. L., B. Langebrunner, J. D. Neelin, and A. Hall, 2018: Increasing precipitation volatility in twenty-first-century California. *Nat. Climate Change*, **8**, 427–433, https://doi.org/10.1038/s41558-018-0140-y.

Wallace, J. M., and D. S. Gutzler, 1981: Teleconnections in the geopotential height field during the Northern Hemisphere winter. *Mon. Wea. Rev.*, **109**, 784–812, https://doi.org/10.1175/1520-0493(1981)109<0784:TITGHF>2.0.CO;2.

Wang, H., S. D. Schubert, and R. D. Koster, 2017: North American drought and links to northern Eurasia: The role of stationary Rossby waves. *Climate Extremes: Patterns and Mechanisms*, *Geophys. Monogr.*, Vol. 226, Amer. Geophys. Union, 197–220, https://doi.org/10.1002/9781119068020.ch12.

Wang, S.-Y., J. H. Yoon, E. Becker, and R. Gillies, 2017: California from drought to deluge. *Nat. Climate Change*, **7**, 465–468, https://doi.org/10.1038/nclimate3330.

Yu, B., and H. Lin, 2019: Modification of the wintertime Pacific–North American pattern related North American climate anomalies by the Asian–Bering–North American teleconnection. *Climate Dyn.*, **53**, 313–328, https://doi.org/10.1007/s00382-018-4586-4.